











A Comprehensive Study of Galaxies at $z \sim 9$ –16 Found in the Early JWST Data: Ultraviolet Luminosity Functions and Cosmic Star Formation History at the Pre-reionization Epoch

Yuichi Harikane¹ , Masami Ouchi^{1,2,3} , Masamune Oguri^{4,5} , Yoshiaki Ono¹ , Kimihiko Nakajima² , Yuki Isobe^{1,6} ,
Hiroya Umeda^{1,6}, Ken Mawatari² , and Yechi Zhang^{1,7} 

¹ Institute for Cosmic Ray Research, The University of Tokyo, 5-1-5 Kashiwanoha, Kashiwa, Chiba 277-8582, Japan; hari@icrr.u-tokyo.ac.jp

² National Astronomical Observatory of Japan, 2-21-1 Osawa, Mitaka, Tokyo 181-8588, Japan

³ Kavli Institute for the Physics and Mathematics of the Universe (WPI), University of Tokyo, Kashiwa, Chiba 277-8583, Japan

⁴ Center for Frontier Science, Chiba University, 1-33 Yayoi-cho, Inage-ku, Chiba 263-8522, Japan

⁵ Department of Physics, Graduate School of Science, Chiba University, 1-33 Yayoi-cho, Inage-ku, Chiba 263-8522, Japan

⁶ Department of Physics, Graduate School of Science, The University of Tokyo, 7-3-1 Hongo, Bunkyo, Tokyo 113-0033, Japan

⁷ Department of Astronomy, Graduate School of Science, The University of Tokyo, 7-3-1 Hongo, Bunkyo, Tokyo 113-0033, Japan

Received 2022 August 2; revised 2022 December 2; accepted 2022 December 9; published 2023 February 15

Abstract

We conduct a comprehensive study on dropout galaxy candidates at $z \sim 9$ –16 using the first 90 arcmin² James Webb Space Telescope (JWST) Near Infrared Camera images taken by the early release observations (ERO) and early release science programs. With the JWST simulation images, we find that a number of foreground interlopers are selected with a weak photo- z determination ($\Delta\chi^2 > 4$). We thus carefully apply a secure photo- z selection criterion ($\Delta\chi^2 > 9$) and conventional color criteria with confirmations of the ERO Near Infrared Spectrograph spectroscopic redshifts, and obtain a total of 23 dropout galaxies at $z \sim 9$ –16, including two candidates at $z_{\text{phot}} = 16.25^{+0.24}_{-0.46}$ and $16.41^{+0.66}_{-0.55}$. We perform thorough comparisons of dropout galaxies found in our work with recent JWST studies, and conclude that our galaxy sample is reliable enough for statistical analyses. We derive the UV luminosity functions at $z \sim 9$ –16, and confirm that our UV luminosity functions at $z \sim 9$ and 12 agree with those determined by other Hubble Space Telescope and JWST studies. The cosmic star formation rate (SFR) density decreases from $z \sim 9$ to 12, and perhaps to 16, but the densities at $z \sim 12$ –16 are higher than the constant star formation efficiency model. Interestingly, there are six bright galaxy candidates at $z \sim 10$ –16 with $M_{\text{UV}} < -19.5$ mag and $M_* \sim 10^{8-9} M_{\odot}$. Because a majority ($\sim 80\%$) of these galaxies show no signatures of active galactic nuclei in their morphologies, the high cosmic SFR densities and the existence of these UV-luminous galaxies are explained by the lack of suppression of star formation by the UV background radiation at the pre-reionization epoch and/or an efficient UV radiation production by a top-heavy initial mass function with Population III-like star formation.

Unified Astronomy Thesaurus concepts: [Galaxy evolution \(594\)](#); [Galaxy formation \(595\)](#); [High-redshift galaxies \(734\)](#)

1. Introduction

One of the most important goals in astronomy today is to understand galaxy formation from the birth stage to the current stage (Stark 2016; Dayal & Ferrara 2018; Ouchi et al. 2020; Robertson 2022). To accomplish the goal, observations for present galaxies to first galaxies are key to revealing the entire process of galaxy formation, while observations of early high-redshift galaxies, especially first galaxies, are missing (e.g., Zackrisson et al. 2011; Nakajima & Maiolino 2022).

Over the past 2–3 decades, large telescopes have driven observational studies of galaxy formation with millions of galaxies at a redshift up to $z \sim 10$ since the start of deep-field imaging observations represented by the legendary Hubble Deep Field project with the Hubble Space Telescope (HST; Williams et al. 1996). To date, deep-field imaging observations have reached detection limits of $\simeq 30$ mag in the wavelength range of 0.4–1.6 μm with the HST Advanced Camera for Surveys (ACS) and the Wide Field Camera 3 (WFC3)

instruments in the Hubble Ultra Deep Field (Beckwith et al. 2006; see Bouwens et al. 2021 and references therein) with the moderately deep ultraviolet (UV) extension, UVUDF (0.2–0.4 μm ; Windhorst et al. 2011; Teplitz et al. 2013). Albeit with shallower detection limits of ~ 26 –29 mag, the HST Great Observatories Origins Deep Survey, the Cosmological Evolution Survey (COSMOS), the Cosmic Assembly Near-infrared Deep Extragalactic Legacy Survey (CANDELS), and the associated parallel-field programs have covered a total area of square degrees in the blank fields (Giavalisco et al. 2004; Scoville et al. 2007; Grogin et al. 2011; Koekemoer et al. 2011). Complementary ground-based observations of the Subaru Hyper Suprime-Cam survey have completed optical imaging covering ~ 1000 deg² with a ~ 26 mag depth (Aihara et al. 2022; see also Harikane et al. 2022b), while the ground-based near-infrared (1–2 μm) and Spitzer Space Telescope imaging (3–8 μm) are limited to a total of few square degrees with similar or moderate depths of ~ 25 –26 mag. Beyond deep imaging in blank fields, the HST programs, the Hubble Frontier Fields (HFF) and the Reionization Lensing Cluster Survey (RELICS), target 6 and 41 massive clusters, respectively, with depths of ~ 26 –29 mag to study faint high-redshift galaxies behind the clusters, exploiting gravitational lensing

magnification (Lotz et al. 2017; Coe et al. 2019). These deep imaging data provide more than 4 million photometrically selected dropout galaxies at $z \sim 4\text{--}10$ (Bouwens et al. 2021; Harikane et al. 2022b) and up to $z \sim 13$ (Harikane et al. 2022a). Albeit with very small high-redshift galaxy samples, spectroscopic observations confirm galaxies up to $z = 9.1$ with the Atacama Large Millimeter/submillimeter Array (ALMA; Hashimoto et al. 2018) and $z = 11.0$ by HST/WFC3 grism and Keck Multi-Object Spectrometer For Infra-Red Exploration (MOSFIRE) spectroscopy (Oesch et al. 2016; Jiang et al. 2021). Star formation in even higher redshift ($z \gtrsim 14$) is discussed based on Balmer-break galaxy candidates at $z \sim 6$ (Mawatari et al. 2020a).

With the galaxy samples photometrically selected in the rest-frame UV wavelengths, a number of studies have derived rest-frame UV luminosity functions reaching up to $z \sim 10\text{--}13$. The UV luminosity functions show the redshift evolution from $z \sim 3$ to 10 with a decrease in the normalization ϕ^* and an increase in the faint-end slope α , and no evolution of characteristic luminosity L^* on the basis of the Schechter function parameterization (Bouwens et al. 2015, 2021; Finkelstein et al. 2015a; Ishigaki et al. 2018). At $z \sim 4$ and above, there are claims that the bright end of the UV luminosity function is explained with the double-power-law function, but not with the Schechter function, due to the excessive number of bright galaxies (Bowler et al. 2014, 2020; Ono et al. 2018; Stevans et al. 2018; Harikane et al. 2022b). Such bright galaxy population includes galaxies with spectroscopic redshifts at $z \sim 10$ (Oesch et al. 2016; Jiang et al. 2021) and perhaps galaxy candidates at $z \sim 13$ (Harikane et al. 2022a), while it is not clearly concluded with sufficient statistical accuracy and spectroscopic confirmations (e.g., Stefanon et al. 2019; Bowler et al. 2020; Rojas-Ruiz et al. 2020).

Over cosmological volumes, the redshift evolution of the cosmic star formation rate (SFR) density is revealed by the UV luminosity function measurements and shows a monotonic decrease from $z \sim 3$ to $z \sim 10$ with a small contribution of dusty starbursts at $z \gtrsim 6$ (e.g., Barrufet et al. 2022; Bouwens et al. 2022a). The UV luminosity function measurements provide the physical picture of galaxy formation over the redshift range of $z \sim 0\text{--}10$, tying galaxies and dark matter halos via abundance-matching techniques (e.g., Behroozi et al. 2013, 2019; Moster et al. 2013, 2018; Finkelstein et al. 2015b). There is an increasing trend of the stellar-to-halo mass ratio toward high redshift for a given halo mass (e.g., Behroozi et al. 2013, 2019; Harikane et al. 2016, 2018), which is consistent with the original idea of the galaxy formation downsizing picture (Cowie et al. 1988). The galaxy–dark matter halo connection probed by the clustering analysis indicates that the star formation efficiency, defined by the ratio of the SFR to the dark matter accretion rate, SFR/\dot{M}_h , is almost constant across redshift values of $z \sim 2\text{--}7$ given the dark matter halo mass (Harikane et al. 2018, 2022b), and the constant star formation efficiency model can reproduce the evolutionary trend of the cosmic SFR density (e.g., Bouché et al. 2010; Mason et al. 2015; Harikane et al. 2018, 2022b; Tacchella et al. 2018).

The UV luminosity function measurements, especially at the faint end, are clue to understanding galaxy formation (Yue et al. 2016) as well as cosmic reionization (Robertson 2022), where abundant faint star-forming galaxies are thought to be sources of cosmic reionization. The faint-end ($\gtrsim -15$ mag) UV luminosity function at $z \sim 6\text{--}10$ is probed with galaxies behind

massive clusters, e.g., with HFF data, via gravitational lensing magnification (Atek et al. 2015, 2018; Ishigaki et al. 2015, 2018; Laporte et al. 2016; Livermore et al. 2017; Oesch et al. 2018), while the faint-end slopes and luminosity function turnovers are poorly constrained due to the limited statistics and lensing magnification systematics (Bouwens et al. 2017, 2022a; Kawamata et al. 2018; Yang et al. 2022).

The James Webb Space Telescope (JWST) was launched in the end of 2021 and started its operation in early 2022. The first data sets of JWST were released on 2022 July 12, taken by the early release observations (ERO), whose targets include a massive cluster SMACS J0723.3-7327 (SMACS J0723, $z = 0.39$) and Stephan’s Quintet. The ERO imaging data taken with the NIRCcam (Rieke et al. 2005) are deep enough to detect high-redshift galaxies with depths of ~ 30 mag, and multiband data covering $\gtrsim 2 \mu\text{m}$ wavelengths allow us to detect galaxies at a previously unreachable redshift range of up to $z \sim 20$. Rest-frame optical emission at $z \gtrsim 10$ is redshifted to the mid-infrared bands and can be covered with the Mid-Infrared Instrument (MIRI; Bouchet et al. 2015). The ERO spectroscopic data of the NIRSpec (Jakobsen et al. 2022) taken in the multiobject spectroscopy mode confirmed galaxies up to $z = 8.5$ with rest-frame optical lines in the $2\text{--}5 \mu\text{m}$ wavelengths. The Near Infrared Imager and Slitless Spectrograph (NIRISS; Doyon et al. 2012) supplements spectroscopic redshift determinations in the wavelength range of $\sim 1\text{--}2 \mu\text{m}$. All of these data sets are revolutionizing galaxy formation studies. The JWST observatory subsequently releases the director’s discretionary early release science (ERS) data, which include NIRCcam, NIRSpec, and NIRISS data taken by the ERS programs of the Cosmic Evolution Early Release Science (CEERS; Finkelstein et al. 2017, 2022c) and GLASS JWST Early Release Science (GLASS; Treu et al. 2022). Further releases will deliver data of Cycle 1 observations that include the Public Release IMaging for Extragalactic Research (PRIMER; Dunlop et al. 2021), the Ultra-deep NIRCcam and NIRSpec Observations Before the Epoch of Reionization (UNCOVER; Labbe et al. 2021), and COSMOS-Webb (Kartaltepe et al. 2021) once the observations are completed. Programs of guaranteed-time observations (GTO), such as the JWST Advanced Deep Extragalactic Survey (JADES; Bunker et al. 2020), will be also completed in the early years.

This is a great development of observational astronomy, presenting the unprecedentedly deep and high-quality data covering the infrared band ($> 2 \mu\text{m}$). In fact, after the releases of the ERO and ERS data sets, we find an explosive progress of galaxy formation studies. The mass models of the ERO target cluster, SMACS J0723, are improved with the NIRCcam imaging and NIRSpec spectroscopic data (Caminha et al. 2022; Mahler et al. 2022; Pascale et al. 2022). High-redshift galaxies are searched in the ERO SMACS J0723 and ERS CEERS and GLASS fields, and are identified at $z \sim 9\text{--}20$ (Adams et al. 2023; Atek et al. 2023; Castellano et al. 2022; Donnan et al. 2023; Finkelstein et al. 2022b; Leethochawalit et al. 2022; Morishita & Stiavelli 2022; Naidu et al. 2022b; Yan et al. 2023). The morphological properties are investigated with the NIRCcam images of the ERO SMACS J0723 and the CEERS observations via the comparisons of HST images for galaxies at $z \sim 3\text{--}6$ (Ferreira et al. 2022) and the rest-frame optical and near-infrared bands for galaxies at $z \sim 1\text{--}2$ (Suess et al. 2022), respectively. The infrared photometric properties

Table 1
Limiting Magnitudes of the JWST Data

Field (1)	Area (arcmin ²) (2)	5σ Limiting Magnitude							
		F090W (3)	F115W (4)	F150W (5)	F200W (6)	F277W (7)	F356W (8)	F410M (9)	F444W (10)
SMACS J0723	11.0	29.4	...	29.4	29.6	29.8	29.9	...	29.6
GLASS	6.8	29.5	29.6	29.4	29.6	29.6	29.9	...	29.6
CEERS1	8.4	...	29.3	29.1	29.3	29.5	29.7	28.9	29.1
CEERS2	8.5	...	29.3	29.0	29.7	29.5	29.6	28.9	29.4
CEERS3	8.4	...	29.4	29.2	29.4	29.6	29.7	29.0	29.2
CEERS6	8.4	...	29.4	29.1	29.3	29.5	29.7	29.0	29.0
Stephan's Quintet	37.2	27.7	...	27.9	28.1	28.8	28.9	...	28.6
PSF FWHM		0".06	0".07	0".07	0".08	0".13	0".14	0".16	0".16

Note. Columns: (1) Field. (2) Effective area in arcmin². (3)–(12) Typical limiting magnitudes that correspond to 5σ variations in the sky flux measured with a circular aperture of 0".2 in diameter in the deepest region.

of galaxies at $z \sim 1$ –2 are studied with the NIRCcam and MIRI images of the ERO SMACS J0723 observations in conjunction with the ALMA archival data (Cheng et al. 2022). The ERO NIRSpec observations in SMACS J0723 provide high-quality spectra that allow us to identify 10 galaxies at $z = 1.2$ –8.5, 3 of which reside at $z = 7.7$ –8.5 (Carnall et al. 2023), and to characterize the interstellar medium of the galaxies (Schaerer et al. 2022; Curti et al. 2023). NIRISS spectroscopic data complements the NIRSpec observations and provide a spectroscopic sample of $z \sim 1$ –8 galaxies (Boyett et al. 2022; Roberts-Borsani et al. 2022; Wang et al. 2022; Marchesini et al. 2023). More JWST results for galaxy formation are being actively reported.

In this paper, we present a comprehensive study on high-redshift galaxies using the first JWST/NIRCcam data sets taken by the ERO and ERS programs. The deep infrared imaging data taken with NIRCcam allow us to search for galaxies at $z \gtrsim 9$ and to constrain the UV luminosity function and the cosmic SFR density in the universe 600 Myr after the Big Bang. We will also perform thorough comparisons of galaxies found in our work and recent JWST studies.

This paper is organized as follows. Section 2 presents the JWST observational data sets used in this study. Section 3 explains our sample selection and galaxy photometry catalog. In Section 4, we describe the mass model for the lensing cluster. We show our main results of UV luminosity functions and cosmic SFR densities in Section 5, and discuss the physical properties of early galaxies in Section 6. Section 7 summarizes our findings. Throughout this paper, we use the Planck cosmological parameter sets of the TT, TE, EE+lowP+lensing+BAO result (Planck Collaboration et al. 2020): $\Omega_m = 0.3111$, $\Omega_\Lambda = 0.6899$, $\Omega_b = 0.0489$, $h = 0.6766$, and $\sigma_8 = 0.8102$. All magnitudes are in the AB system (Oke & Gunn 1983).

2. Observational Data Set

2.1. JWST/NIRCcam Data

We use four JWST NIRCcam data sets obtained in the ERO and ERS programs, ERO SMACS J0723, ERO Stephan's Quintet, ERS CEERS, and ERS GLASS (Table 1). The total area is ~ 90 arcmin². We retrieved raw data (`_uncal.fits`) from the Mikulski Archive for Space Telescopes archive and reduced the data using the JWST pipeline version 1.6.3 development version (1.6.3.dev34+g6889f49, almost the same as 1.7.0). We use the Calibration Reference Data System context file of

`jwst_0995.pmap` released in October, whose calibration values were derived using calibration observations of three different standard stars placed in all of the 10 NIRCcam detectors. These new flux calibrations were verified using imaging of the globular cluster M92 (Boyer et al. 2022). In addition to the standard reduction, we added some processes to obtain better reduced images as follows. Before the Stage 2 calibration, we subtracted stray-light features called “wisps” by using a script provided by the NIRCcam team,⁸ and removed striping by using a script provided in the CEERS team (Bagley et al. 2022a).⁹ We ran the `SkyMatch` step individually on each frame of Stage 2 calibrated data before Stage 3 calibration, following a suggestion by the CEERS team (Bagley et al. 2022a). The images were pixel-aligned with a pixel scale of 0".015 pixel⁻¹, except for ones in the Stephan's Quintet field with a scale of 0".03 pixel⁻¹ to reduce image sizes. Because the pipeline-processed images still showed a gradient of the sky background, we further subtracted the sky background using `SEXTRACTOR` (Bertin & Arnouts 1996). The intracluster light around the cluster center of SMACS J0723 is also removed in this process, although more sophisticated processes are sometimes employed (e.g., Livermore et al. 2017; Pagul et al. 2021). Note that our galaxy samples are not severely affected by systematics due to the intracluster light removal, because as shown in Section 3.5, the only candidate selected in the SMACS J0723 field, SM-z12-1, is located in the parallel field. The results of luminosity functions do not change beyond the errors if we remove the data point estimated with the SMACS J0723 data. Finally, we corrected for an astrometric offset between each detector and band using IRAF tasks `geomap` and `geotran`. To check the reliability of the flux calibration, we compare our measured magnitudes in the JWST images with those in the HST and Spitzer images. As shown in Figure 1, the measured fluxes are almost consistent with those in the HST and Spitzer images, indicating that the flux is reasonably calibrated.

The limiting magnitudes were measured in 0".1, 0".2, and 0".3 diameter circular apertures by randomly placing apertures in sky areas using Python packages `ASTROPY/PHOTUTILS`. Sky areas were defined as pixels without objects detected by `SEXTRACTOR`. We measured the limiting magnitudes in bins of

⁸ <https://jwst-docs.stsci.edu/jwst-near-infrared-camera/nircam-features-and-caveats/nircam-claws-and-wisps>

⁹ <https://ceers.github.io/releases.html#sdr1>

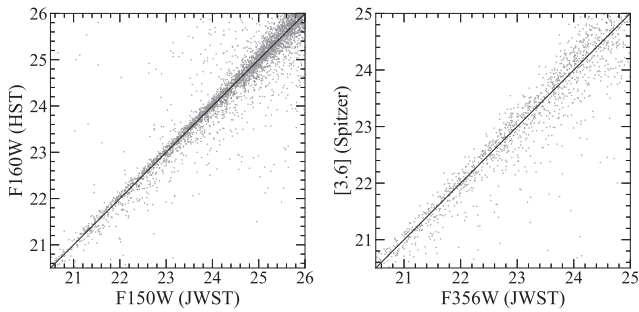


Figure 1. Comparison of magnitudes. Magnitudes measured in the JWST F150W band (left) and F356W band (right) are compared with those in the HST F160W band and Spitzer [3.6] band, respectively. The measured magnitudes agree well with those in the HST and Spitzer images within $\sim 10\%$, indicating that the flux is reasonably calibrated. Note that we include a 10% error floor on all measured fluxes to account for possible systematic uncertainties.

the weight values to take the inhomogeneity of the depth into account. Using the weight map, we masked some regions around the edge of the detectors whose exposure time is short. We also measured the FWHM of the point-spread function (PSF) in each image by selecting stellar objects in the magnitude–FWHM diagram. The measured limiting magnitudes in a $0''.2$ diameter circular aperture, effective areas, and typical FWHMs of the PSFs are presented in Table 1. Here the effective area is defined as an area that is observed with all available bands before the foreground removal. The effect of the foreground will be taken into account in the completeness estimate (Section 5.1). In the following sections we detail our observational data set in each field.

2.1.1. ERO: SMACS J0723

A massive galaxy cluster at $z = 0.39$, SMACS J0723, was deeply observed with NIRCcam, NIRSpec, MIRISS, and MIRI in the ERO (ERO-2736). The NIRCcam images were taken in the six bands of F090W, F150W, F200W, F277W, F356W, and F444W, covering 11.0 arcmin^2 . The exposure time in each filter is $\sim 7500 \text{ s}$, and the 5σ limiting magnitude in the F356W band is 29.9 mag.

2.1.2. ERO: Stephan’s Quintet

Stephan’s Quintet, a group of five local galaxies, was observed with NIRCcam and MIRI in the ERO (ERO-2732). The NIRCcam images were taken in the six bands of F090W, F150W, F200W, F277W, F356W, and F444W, covering 42 arcmin^2 . We have masked central regions of the field that is affected by the five local galaxies in Stephan’s Quintet, resulting in an effective area of 37.2 arcmin^2 , corresponding to ~ 4 NIRCcam pointings. The exposure time in each filter is roughly $\sim 1200 \text{ s}$, and the 5σ limiting magnitude in the F356W band is 28.9 mag.

2.1.3. ERS: CEERS

A part of the HST/CANDELS Extended Groth Strip (EGS) field is observed with JWST in the CEERS survey (ERS-1345; Finkelstein et al. 2017, 2022c). We use four pointing data sets of NIRCcam obtained in 2022 June with the seven bands of F115W, F150W, F200W, F277W, F356W, F410M, and F444W, covering a total of 33 arcmin^2 . The exposure time in each filter is $\sim 2800\text{--}6200 \text{ s}$, and the 5σ limiting magnitude in

the F356W band is 29.7 mag. As the exposure times are not uniform across the four NIRCcam pointings, we separately analyze the four pointing data.

2.1.4. ERS: GLASS

A massive galaxy cluster, A2744, was observed with JWST in the ERS program of Through the Looking GLASS (ERS-1324; Treu et al. 2017, 2022). Deep NIRCcam images were taken in 2022 June in a parallel mode of NIRISS observations targeting the center of the cluster, in seven bands F090W, F115W, F150W, F200W, F277W, F356W, and F444W, covering 6.8 arcmin^2 . The exposure time in each filter is $\sim 5600\text{--}23,000 \text{ s}$, and the 5σ limiting magnitude in the F356W band is 29.9 mag. The lensing magnification is negligible in the field of the NIRCcam observations that is $\sim 5'$ away from the cluster center of A2744.

2.2. JWST/NIRSpec

We use publicly available data from the ERO NIRSpec observations targeting the field of the SMACS J0723 cluster (ERO-2736). The NIRSpec observations consist of two pointings with the same multi-shutter array (MSA) configuration. NIRSpec observations were carried out by using the disperser-filter combinations of G235M/F170LP and G395M/F290LP, which cover the wavelength range from 1.66 to $5.16 \mu\text{m}$ with a spectral resolution of $R \sim 1000$. The total exposure time of the two individual pointings is 8840 s for each grating. The NIRSpec observations have taken spectra for a total of 35 objects, 3 of which, s04590 ($z_{\text{spec}} = 8.495$), s06355 ($z_{\text{spec}} = 7.664$), and s10612 ($z_{\text{spec}} = 7.659$), are securely identified at $z > 7$ whose dropouts can be covered with the NIRCcam F090W band. See Nakajima et al. (2023) for details on the reduction and analysis of the NIRSpec data.

2.3. HST/ACS and WFC3

HST multiband images are available in the fields of SMACS J0723 and CEERS (EGS). We downloaded HST ACS and WFC3 images in the SMACS J0723 and CEERS fields from the websites of RELICS (Coe et al. 2019)¹⁰ and CEERS¹¹ respectively. We found a small offset ($\sim 0''.2$) of the WCS between the JWST and HST images. In this paper we use coordinates of the JWST images.

3. Photometric Catalog and Sample Selection

3.1. Photometric Catalog

We construct multiband source catalogs from the JWST data to select the F115W, F150W, and F200W-dropout galaxies. We use SWARP (Bertin et al. 2002) to produce our detection image that is a weighted mean image of the bands redder than the Lyman break in each dropout selection (i.e., F150W, F200W, F277W, F356W, F410M, and F444W for the F115W-dropout selection, F200W, F277W, F356W, F410M, and F444W for the F150W-dropout selection, and F277W, F356W, F410M, and F444W for the F200W-dropout selection). To measure object colors, we match the image PSFs to the F444W-band images whose typical FWHM of the PSF is $\sim 0''.16$, the largest of the NIRCcam multiband images.

¹⁰ <https://archive.stsci.edu/prepds/relics/#dataaccess>

¹¹ <https://ceers.github.io/releases.html#hdr1>

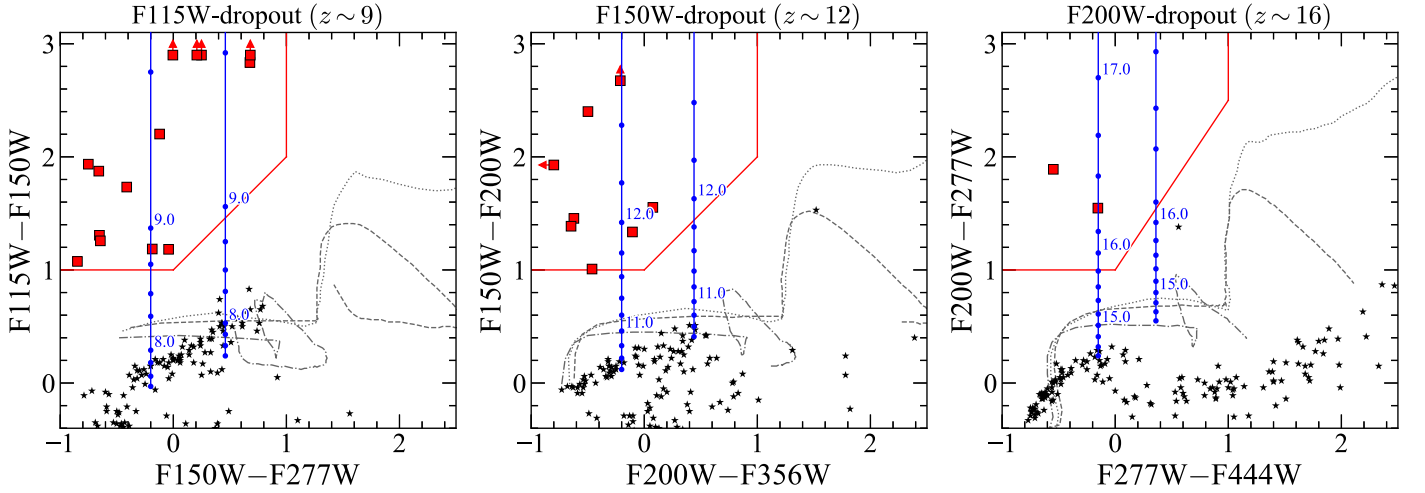


Figure 2. Two-color diagrams of F115W – F150W vs. F150W – F277W (left), F150W – F200W vs. F200W – F356W (center), and F200W – F277W vs. F277W – F444W (right) corresponding to the color selections for F115W dropouts at $z \sim 9$, F150W dropouts at $z \sim 12$, and F200W dropouts at $z \sim 16$, respectively. The red squares represent our dropout galaxy candidates that meet the color selection criteria indicated with the red lines. The blue lines denote colors of the dropout galaxy models with UV spectral slopes of $\beta_{UV} = -2.3$ and -1.3 whose redshifts are indicated with the numbers and the blue circles with an interval of $\Delta z = 0.2$. The black dotted, dashed, and dotted–dashed lines show colors of typical elliptical, Sbc, and irregular galaxies (Coleman et al. 1980) redshifted from $z = 0$ to 7. The star marks present the expected colors of Galactic dwarf stars (Patten et al. 2006; Kirkpatrick et al. 2011). These colors of dwarf stars are estimated by interpolating the available flux measurements obtained by ground-based telescopes (J , H , and K bands) and the Spitzer telescope ([3.6] and [4.5]).

We perform source detection and photometry with SEXTRACTOR (version 2.5.0; Bertin & Arnouts 1996). We found that the photometry with SEXTACTOR `MAG_AUTO` performs better as a total magnitude than that with photutils `iso-phototal_flux`, which is one of the outputs of the JWST calibration pipeline, using CEERS-simulated images with a mock galaxy catalog created with the Santa Cruz Semi-Analytic Model (Somerville et al. 2021; Yung et al. 2022).¹² We run SEXTRACTOR in the dual-image mode for each image with its detection image, having the parameter set as follows: `DETECT_MINAREA = 5`, `DETECT_THRESH = 3.0`, `ANALYSIS_THRESH = 3.0`, `DEBLEND_NTHRESH = 32`, and `DEBLEND_MINCOUNT = 0.005`. The total number of the objects detected is $\sim 250,000$. We measure the object colors with the `MAG_APER` magnitudes defined in a $0''.3$ diameter circular aperture in the PSF-matched images. Source detections are evaluated with $0''.1$ and/or $0''.2$ diameter circular apertures in the original (not PSF-matched) images. The total magnitudes are estimated from the $0''.3$ diameter aperture magnitudes with the aperture correction. The value of the aperture correction is defined as the difference between the `MAG_AUTO` magnitude and the $0''.3$ diameter aperture magnitude in an image of the weighted mean of the PSF-matched images whose wavelengths are longer than the Lyman break (i.e., F150W, F200W, F277W, F356W, F410M, and F444W for the F115W-dropout selection, F200W, F277W, F356W, F410M, and F444W for the F150W-dropout selection, and F277W, F356W, F410M, and F444W for the F200W-dropout selection). Furthermore, we correct for a small offset (~ 0.1 mag) between the measurement of `MAG_AUTO` and the true total magnitude due to the wing of the PSF not captured with `MAG_AUTO` (see Sections 2.2 and 2.5.1 in Finkelstein et al. 2022a). We measure this offset by randomly inserting mock galaxy images in the real images, and measure the magnitudes using SEXTRACTOR in a similar manner as the completeness simulation described later in Section 5.1. To account for systematic uncertainties of

the flux measurements (e.g., zero-point correction), we include a 10% error floor on all measured fluxes. Finally we correct for the galactic extinction using Schlegel et al. (1998) and Schlafly & Finkbeiner (2011) and make final photometric catalogs.

3.2. Dropout Selection

From the photometric catalogs constructed in Section 3.1, we construct $z \sim 9$ – 16 dropout galaxy catalogs based on the Lyman break color selection technique (e.g., Steidel et al. 1996; Giavalisco 2002). As shown in Figure 2, galaxy candidates at $z \sim 9$, 12, and 16 can be selected by the F115W, F150W, and F200W-dropout selections, respectively.

First, to identify secure sources, we select sources whose signal-to-noise ratios (S/Ns) in a $0''.2$ diameter circular aperture are higher than 5 in the detection images. We also require sources to be detected at $>3.5\sigma$ levels in at least two bands redder than the Lyman break. We then select dropout galaxy candidates by using their broadband spectral energy distribution (SED) colors. We adopt the following color criteria: F115W dropout ($z \sim 9$):

$$(F115W - F150W > 1.0) \wedge , \quad (1)$$

$$(F150W - F277W < 1.0) \wedge , \quad (2)$$

$$(F115W - F150W > (F150W - F277W) + 1.0); \quad (3)$$

F150W dropout ($z \sim 12$):

$$(F150W - F200W > 1.0) \wedge , \quad (4)$$

$$(F200W - F356W < 1.0) \wedge , \quad (5)$$

$$(F150W - F200W > (F200W - F356W) + 1.0); \quad (6)$$

F200W dropout ($z \sim 16$):

$$(F200W - F277W > 1.0) \wedge , \quad (7)$$

$$(F277W - F444W < 1.0) \wedge , \quad (8)$$

$$(F200W - F277W > 1.5(F277W - F444W) + 1.0). \quad (9)$$

We select sources with prominent breaks with the criteria of Equations (1), (4), and (7), and measure the slope of the continuum and remove red interlopers with Equations (2)–(3),

¹² <https://ceers.github.io/releases.html#sdr1>

(5)–(6), and (8)–(9). To measure the slope of the continuum, we use the bands that have a large wavelength difference as much as possible, while not biting the Balmer break in the redder band. To remove foreground interlopers, we exclude sources with continuum detections at $>2\sigma$ levels in the $0''.1$ or $0''.2$ diameter apertures in bands bluer than the Lyman break, i.e., the F090W band for the F115W dropouts, F090W and F115W bands for the F150W dropouts, and F090W, F115W, and F150W bands for the F200W dropouts. To select reliable candidates, we restrict our dropout selections in fields where bands bluer than the Lyman break are available; the F115W-dropout selection is only performed in the GLASS field. We also apply a criterion of a SEXTRACTOR stellerity parameter, CLASS_STAR, of <0.9 , to remove stellar contaminants. Finally, we visually inspect images of the selected sources to remove spurious sources or sources affected by nearby bright objects and diffraction spikes of bright stars. We removed about half of the selected objects in this process. We also visually inspect HST images of the selected sources in the SMACS J0723 and CEERS fields to check whether the source is consistent with being a high-redshift galaxy, although the HST images are typically ~ 1 – 2 mag shallower than the JWST images in these fields.

3.3. Spectral Energy Distribution Fitting

To further remove low-redshift interlopers, we perform galaxy SED fitting with the flexible Bayesian inference code PROSPECTOR (Johnson et al. 2021) and derive the photometric redshift. Model spectra are derived from Flexible Stellar Population Synthesis (Conroy et al. 2009; Conroy & Gunn 2010) package with the modules for Experiments in Stellar Astrophysics Isochrones and Stellar Tracks (MIST; Choi et al. 2016). The boost of ionizing flux production of massive stars are included in the MIST isochrones (Choi et al. 2017). Here we assume the stellar initial mass function (IMF) determined by Chabrier (2003), the Calzetti et al. (2000) dust extinction law, and the intergalactic medium (IGM) attenuation model by Madau (1995). Note that the choice of the IGM attenuation model does not affect our galaxy selection at $z \sim 9$ – 16 because flux bluer than the Ly α break is almost entirely absorbed by the highly neutral IGM at these redshifts regardless of the choice of the IGM attenuation model. The Ly α emission line is also masked considering the high IGM neutral fraction at these redshifts. We adopt a flexible star formation history with five bins that are spaced equally in logarithmic times between 0 Myr and a look-back time that corresponds to $z = 30$, where the SFR within each bin is constant. We change the redshift, optical depth in the V band, star formation history, and total stellar mass as free parameters, while fix the metallicity to $Z = 0.2 Z_{\odot}$. We assume a continuity prior for the star formation history, and flat priors for other parameters in the range $0 < z < 20$, $0 < \tau_V < 2$, and $6 < \log(M_*/M_{\odot}) < 12$. We search for the best-fit model to the observed photometry with the Markov Chain Monte Carlo (MCMC) method by using EMCEE (Foreman-Mackey et al. 2013).

Based on the results of the SED fitting, we select objects whose high-redshift solution is more likely than the low-redshift one, by using $\Delta\chi^2$, which is defined as the difference between the χ^2 values of the best high-redshift solution and the lower-redshift solution, $\Delta\chi^2 = \chi^2(z_{\text{low}}) - \chi^2(z_{\text{high}})$. Previous studies use a criterion of $\Delta\chi^2 > 4.0$, corresponding to a 2σ

level (e.g., Bowler et al. 2020; Donnan et al. 2023; Finkelstein et al. 2022b; Harikane et al. 2022a). However, given the small number of the available JWST bands that are bluer than the Lyman break and the expected small number density of $z > 9$ galaxies, it is possible that this criterion is not sufficient to remove low-redshift interlopers. To determine the threshold value for $\Delta\chi^2$, we use the CEERS-simulated NIRCcam images. In the CEERS-simulated images, mock galaxies at $z = 0$ – 10 in Yung et al. (2019, 2022) are inserted using the JWST data simulator MIRAGE (Hilbert et al. 2019). We measure fluxes of mock galaxies in each band in the same manner as our real dropout galaxy selection (Section 3.1) and conduct the SED fitting using PROSPECTOR. As shown in Figure 3, at least eight sources at $z_{\text{true}} \sim 3$ – 4 in the simulations have the best photometric redshifts of $z_{\text{phot}} \sim 12$ – 15 and $\Delta\chi^2 = 4$ – 9 , indicating that the criterion of $\Delta\chi^2 > 4$ is not sufficient to remove low-redshift interlopers. Thus in this study, we instead adopt a strict screening criterion of $\Delta\chi^2 > 9.0$, which can remove these interlopers. The inclusion of this strict criterion does not introduce a bias with respect to a color of the UV continuum for bright galaxies, because the strength of the break is the most important factor to determine the $\Delta\chi^2$ value. For faint galaxies, about 40% of them at ~ 29 – 30 mag will be missed due to the inclusion of this criterion, and this effect is taken into account for the completeness estimate in Section 5.1.

3.4. Comparisons with Spectroscopic Redshifts

To test the reliability of our galaxy selections and SED fitting, we compare our photometric redshift estimates with the spectroscopic results obtained in the NIRSspec observations (Section 2.2). As there are currently no $z > 9$ source spectroscopically confirmed with NIRSspec in the fields used in this study, we focus on the three galaxies at $z > 7$, s04590 ($z_{\text{spec}} = 8.495$), s06355 ($z_{\text{spec}} = 7.664$), and s10612 ($z_{\text{spec}} = 7.659$). We measure the fluxes of the three galaxies in the NIRCcam images and estimate the photometric redshifts using PROSPECTOR, in the same manner as our dropout galaxies. Figures 4 and 5 present results of the SED fitting and comparison with the spectroscopic redshifts. We found that the estimated photometric redshifts agree well with the spectroscopic redshifts within $\sim 2\sigma$ uncertainties, indicating that our SED fitting works well to estimate the redshift from the NIRCcam photometry.

3.5. Final Sample

Finally we select 13, 8, and 2 dropout galaxy candidates at $z \sim 9$, 12, and 16, respectively (Table 2). The photometric redshifts range from $z \sim 8.7$ to 16.4, demonstrating the power of JWST exploring the early universe (Figure 6). Examples of the snapshots and SEDs of the selected galaxies at $z \sim 9$, 12, and 16 are presented in Figures 7 and 8. These sources show a sharp discontinuity around the Lyman break band, a flat or blue continuum, and nondetection in the bluer bands than the break, all of which are consistent with a high-redshift galaxy. The photometric properties of our galaxy candidates are summarized in Tables 3–5. Note that no objects appear in more than one final dropout sample.

To investigate the morphological properties of our galaxy candidates, we fit our galaxy candidates with the Sérsic profile using GALFIT (Peng et al. 2010). We find that some bright candidates, i.e., GL-z9-1, GL-z12-1, CR2-z12-1, CR-z16-1,

Interlopers in Simulations

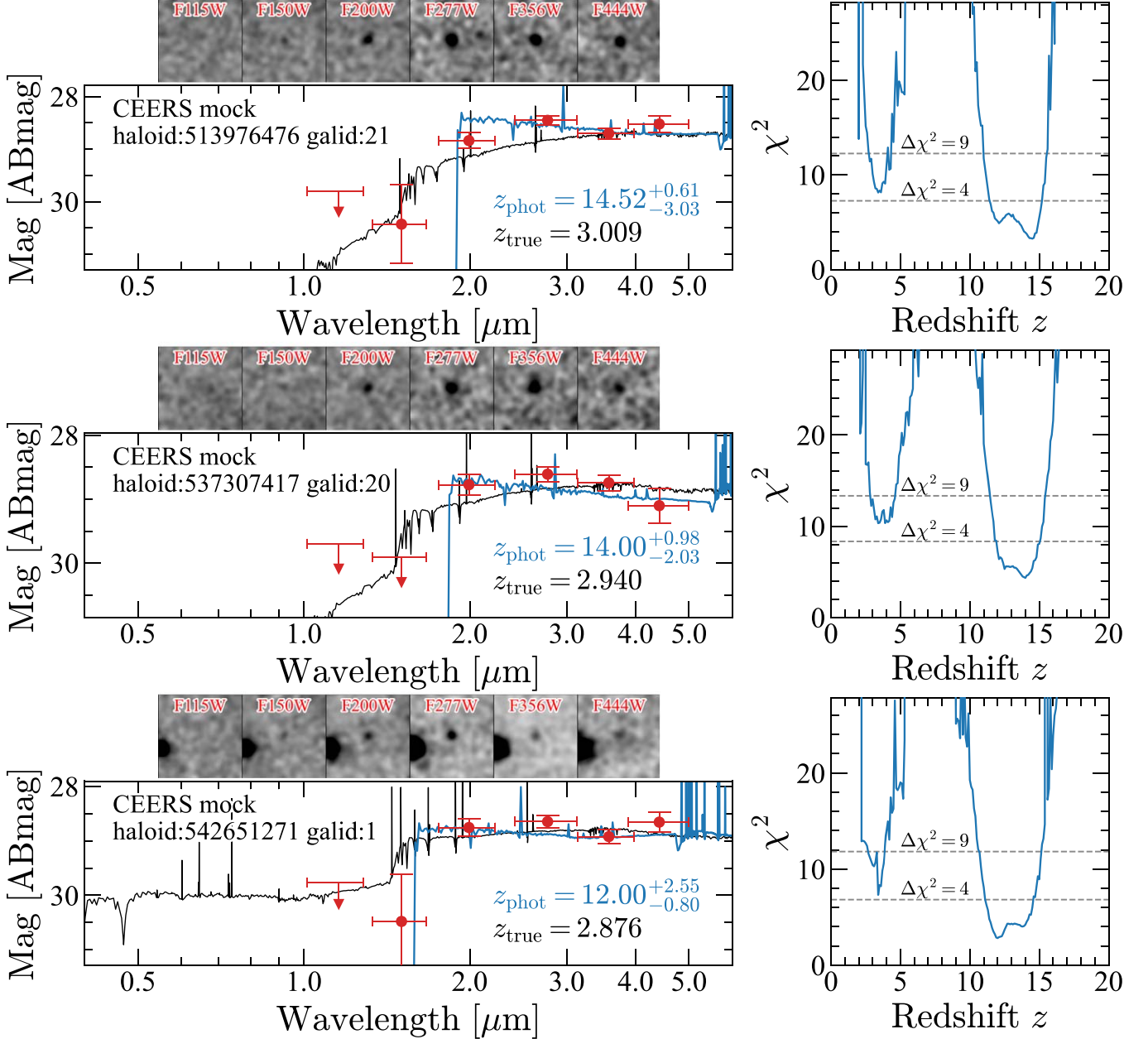


Figure 3. Examples of mock galaxies whose true redshifts are $z_{\text{true}} \sim 3$ but selected as F150W-dropout galaxies at $z_{\text{phot}} \sim 12\text{--}15$ identified in the simulated NIRCcam images. For each object, the top left panel shows the $1''.5 \times 1''.5$ snapshots in NIRCcam bands with a 3 pixel smoothing whose band names are indicated with the red labels. The bottom left panel presents the SED of the object. The red symbols with error bars are the measured magnitudes or 2σ upper limits, and the blue curve shows the best-fit model. The true and estimated redshifts with 2σ errors are indicated with the black and blue texts, respectively. The χ^2 value is shown in the right panel as a function of the redshift. The black curve is the true SEDs at $z \sim 3$, while the blue curve denotes χ^2 values of our SED fitting for our photometric redshift determination. These objects meet the weak photometric redshift criterion of $\Delta\chi^2 > 4$, but do not meet our strict criterion of $\Delta\chi^2 > 9$, where $\Delta\chi^2$ is the χ^2 difference between the best high-redshift solution and a lower-redshift solution, $\Delta\chi^2 = \chi^2(z_{\text{low}}) - \chi^2(z_{\text{high}})$. See the text for details.

and S5-z16-1, are clearly more extended than the PSF, although GL-z12-1 is compact compared to other candidates, implying potential active galactic nucleus (AGN) activity. We stack images of other faint candidates at each redshift and find that the stacked images also show extended profiles with respect to the PSF. We thus conclude that stellar contamination is negligible. Details of the morphological properties of our candidates are presented in Ono et al. (2022).

One of the highest-redshift source candidates in our catalogs is CR2-z16-1 at $z = 16.25^{+0.24}_{-0.46}$ in the CEERS2 field. As

discussed later in Section 3.6.6, CR2-z16-1 is first identified as a $z = 16.4$ source (ID 93116) in Donnan et al. (2023). As shown in the middle panel of Figure 8, our measured fluxes are almost consistent with those presented in Naidu et al. (2022a) and Finkelstein et al. (2022c), while fluxes in Donnan et al. (2023) are systematically fainter than our measurements, probably because Donnan et al. (2023) assume the PSF for the aperture correction. The colors measured in these three studies (this study, Donnan et al. 2023; Naidu et al. 2022a; and Finkelstein et al. 2022c) consistently show a clear break around

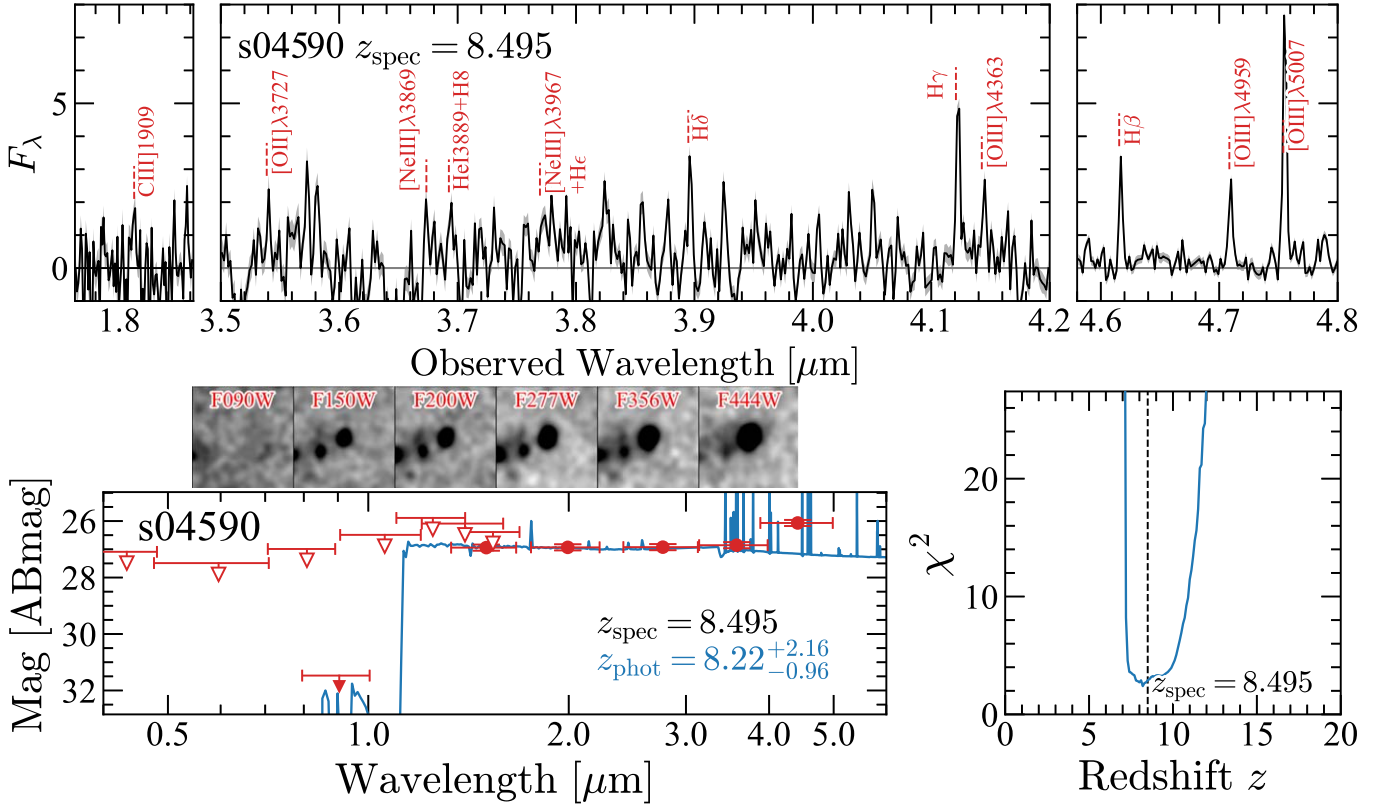


Figure 4. Top: NIRSpect spectrum of s04590 at a spectroscopic redshift of $z = 8.495$. The spectroscopic redshift is confirmed with the H β , H γ , H δ , [O III] $\lambda\lambda$ 5007,4959, [O III] λ 4363, [O II] λ 3727, [Ne III] λ 3967, [Ne III] λ 3869, and tentative C III] λ 1909 lines. The flux is arbitrary. Bottom left: optical to near-infrared SED of s04590. The red circles and arrows indicate the measured magnitudes and 2σ limits, respectively. The filled (open) red symbols denote the measurements and the limits obtained with JWST/NIRCam (HST/ACS and WFC3). The blue curve and the blue redshift label represent the best-fit model SED and the photometric redshift with 2σ errors derived by our photometric redshift technique, which is compared with the spectroscopic redshift indicated with the black label. The images on this panel show $1''.5 \times 1''.5$ cutout images of s04590 in the NIRCams bands with a 3 pixel smoothing whose band names are indicated with the red labels. Bottom right: χ^2 as a function of the redshift. The blue curve denotes χ^2 values of our SED fitting for our photometric redshift determination. The vertical dashed line indicates the spectroscopic redshift that agrees well with the photometric redshift.

the F200W band, consistent with a $z = 16.3$ galaxy, although there are some discussions about a possible solution of a dusty line emitter at $z \sim 5$ (Naidu et al. 2022a; Zavala et al. 2023). Although the NIRSpect spectroscopy is required to conclude the redshift of CR2-z16-1, we include this source as a F200W-dropout galaxy candidate.

The other candidate at $z \sim 17$ is S5-z16-1 at $z = 16.41^{+0.66}_{-0.55}$ identified in the Stephan’s Quintet field. Although this source is located in a region whose exposure time is relatively short compared to the central region of the field, our position-dependent estimates of flux uncertainties indicate that the source detection, color, and nondetections are robust against the uncertainties. An emission line feature is detected with ALMA in S5-z16-1 (Fujimoto et al. 2022), which would be interpreted as either [O III] λ 52 μ m at $z = 16.01$ or [C II] λ 158 μ m at $z = 4.61$. We include this possible candidate in the luminosity function calculation, although the luminosity is remarkably high compared to our expectations at this high redshift.

3.6. Comparison with Previous Studies

Some other studies identified galaxy candidates at $z > 9$ using the JWST NIRCams ERO and/or ERS data sets. Here we review these studies and compare their samples with our galaxy samples. Tables 3–5 summarize properties of other possible candidates that were selected in other studies but did not meet

our selection criteria. These comparisons were conducted on 2022 November 20, and we clarify the version of the paper we compared in the following sections.

3.6.1. Naidu et al. (2022b)

Using the ERS CEERS and GLASS data sets, Naidu et al. (2022b) found two bright galaxy candidates at $z \sim 10$ and 12, GLASS-z10 and GLASS-z12, which correspond to GL-z9-1 and GL-z12-1 in our sample, respectively. Their estimates of the photometric redshifts ($z = 10.35^{+0.38}_{-0.51}$ and $z = 12.38^{+0.13}_{-0.27}$ for GL-z10-1 and GL-z12-1, respectively, with PROSPECTOR, from the ApJL published version) are consistent with our estimates ($z = 10.49^{+0.53}_{-0.72}$ and $z = 12.28^{+0.08}_{-0.07}$).

3.6.2. Castellano et al. (2022)

Castellano et al. (2022) identified seven galaxy candidates at $z \sim 9$ –12 with the color selection using the ERS GLASS data set. Among the six candidates from the version published in *The Astrophysical Journal Letters*, three candidates, GHZ1, GHZ2, and GHZ4, are selected in our selection. GHZ1 (GHZ2) is GL-z9-1 (GL-z13-1) in our sample, and their photometric redshift, $z = 10.53$ –10.63 ($z = 12.11$ –12.30) is comparable with our estimates. GHZ4 was identified in our selection as GL-z9-2, and their photometric redshift ($z = 9.93$ –10.08) agrees with our estimate ($z = 10.46^{+0.45}_{-0.99}$). The other three candidates, GHZ3, GHZ5, and GHZ6, did not meet our selection criteria, due to a

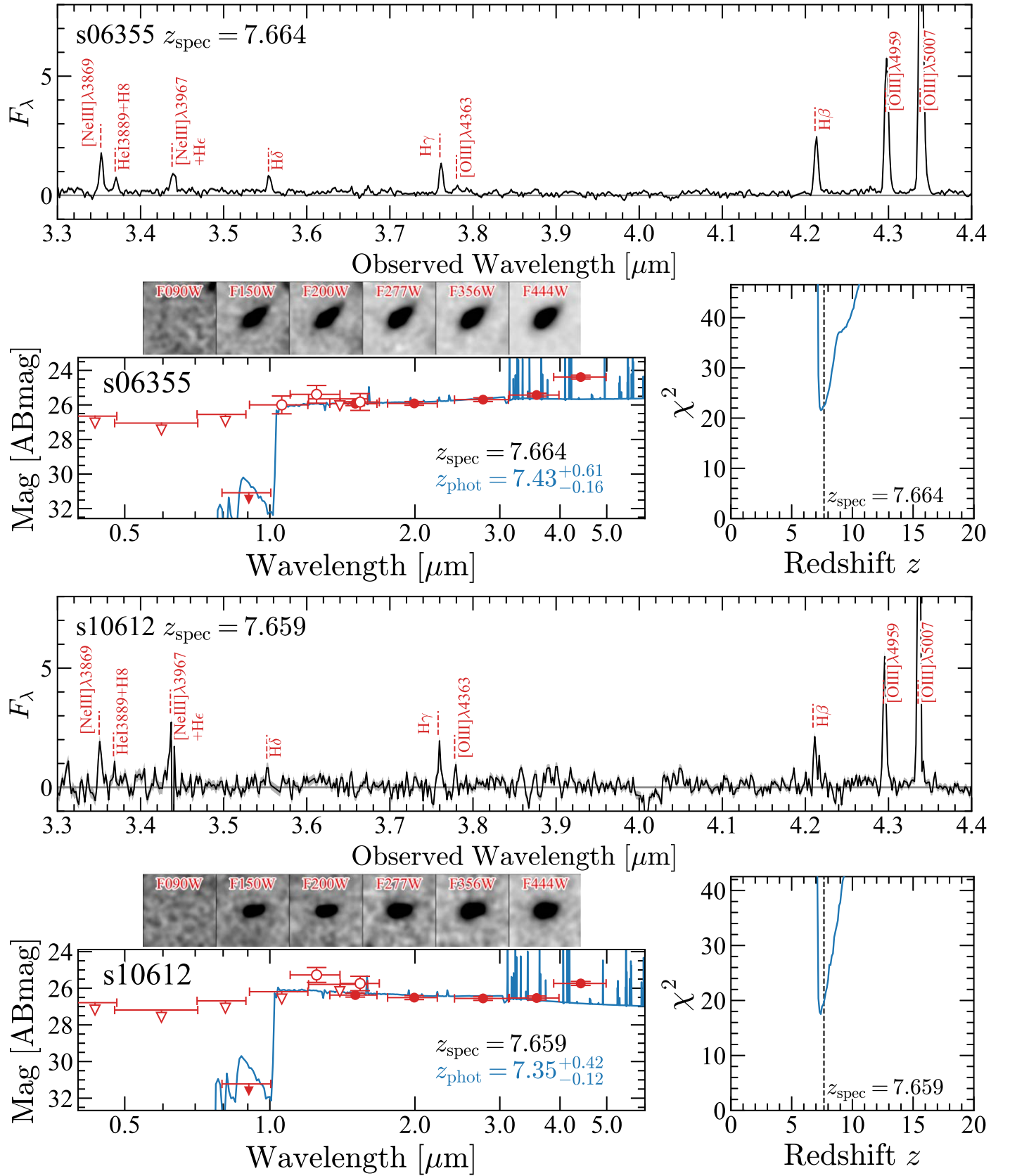


Figure 5. Same as Figure 4, but for s06355 at $z_{\text{spec}} = 7.664$ and s10612 at $z_{\text{spec}} = 7.659$. Our estimates of the photometric redshifts agree well with the spectroscopic redshifts.

possible detection in the F090W band or $\Delta\chi^2 < 9$, although GHZ3 and GHZ5 were also reported to have low-redshift solutions in Castellano et al. (2022).

3.6.3. Leethochawalit et al. (2022)

Leethochawalit et al. (2022) studied photometric properties of galaxies at $7 < z < 9$ using the ERS GLASS data set. We

Table 2
Number of Our Dropout Candidates

Field	F115W dropouts $z \sim 9$	F150W dropouts $z \sim 12$	F200W dropouts $z \sim 16$
SMACS J0723	...	1	0
GLASS	13	1	0
CEERS1	...	0	0
CEERS2	...	4	1
CEERS3	...	1	0
CEERS6	...	0	0
Stephan's Quintet	...	1	1
Total (z)	13	8	2
Total		23	

refer to manuscript version 2, which was submitted to arXiv on October 4. As their galaxies are identified from the F090W-dropout selection, we do not expect significant overlap between their galaxy sample and ours.

3.6.4. Adams et al. (2023)

Adams et al. (2023) identified four galaxy candidates at $9 < z < 12$ in the ERO data set taken in the SMACS J0723 field. We refer to manuscript version 2, which was submitted to arXiv on August 9. As three of them are expected to be at $z < 10$, it is reasonable that they are not identified in our F150W-dropout selection ($z \sim 12$). The other source (ID 10234) is estimated to be at $z = 11.42$, around the edge of our redshift selection window (see Figure 9), and not selected in our study due to its insufficient F150W – F200W color and a possible detection in the F090W band.

3.6.5. Atek et al. (2023)

Using the ERO data set in the SMACS J0723 field, Atek et al. (2023) selected 10 galaxy candidates at $10 < z < 16$. We refer to manuscript version 2, which was submitted to arXiv on October 31. Among them, four candidates, SMACS_z12a, SMAC_z12b, SMACS_z16a, and SMACS_z16b, have photometric redshifts of $z > 12$ and are expected to be overlapped in our galaxy catalogs. However, none of them are selected as high-redshift galaxy candidates in our study, due to their insufficient colors or $\Delta\chi^2 < 9$.

3.6.6. Donnan et al. (2023)

Donnan et al. (2023) selected 45 galaxies at $z > 8.5$ using the ERO SMACS J0723 and ERS GLASS and CEERS data sets. We refer to manuscript version 2, which was submitted to arXiv on October 22. Among the 45 galaxies, 3 galaxies (IDs 1698, 6415, and 17487) are identified in the GLASS data set and are also selected in this study as GL-z9-1, GL-z9-4, and GL-z12-1, respectively. Their photometric redshifts ($z = 10.45^{+0.26}_{-0.16}$, $z = 10.79^{+0.45}_{-0.66}$, and $z = 12.42^{+0.27}_{-0.21}$ for IDs 1698, 6415, and 17487, respectively) are consistent with our estimates ($z = 10.49^{+0.53}_{-0.72}$, $z = 10.19^{+0.63}_{-0.55}$, and $z = 12.28^{+0.08}_{-0.07}$). The brightest candidate in Donnan et al. (2023) is ID 93316 at $z = 16.39^{+0.32}_{-0.22}$, which is CR2-z16-1 at $z = 16.25^{+0.24}_{-0.46}$ in our catalog. In version 2, Donnan et al. (2023) newly selected ID 32395_2 at $z = 12.29^{+0.91}_{-0.32}$, which is also selected in this study as CR2-z12-1 at $z = 11.63^{+0.51}_{-0.53}$ and was first identified in

Finkelstein et al. (2022b). Donnan et al. (2023) presented three other candidates at $z > 12$, but these candidates are not selected in this study due to $\Delta\chi^2 < 9$.

3.6.7. Finkelstein et al. (2022b)

One galaxy candidate at $z \sim 12$, dubbed Maisie's Galaxy in Finkelstein et al. (2022b), is also selected in this study as CR2-z12-1. We refer to manuscript version 2, which was submitted to arXiv on September 7. The photometric redshift presented in Finkelstein et al. (2022b) is $z = 11.8^{+0.3}_{-1.2}$, consistent with our estimate ($z = 11.63^{+0.51}_{-0.53}$).

3.6.8. Yan et al. (2023)

Yan et al. (2023) identified a total of 88 galaxy candidates at $z \sim 11-20$ in the ERO SMACS J0723 field, including 63 F150W dropouts and 15 F200W dropouts, possibly overlapping with our F150W- and F200W-dropout candidates, respectively. We refer to manuscript version 1, which was submitted to arXiv on July 23. Out of 61 and 15 sources in their F150W dropouts and F200W dropouts, we identify 54 and 11 objects in our original photometric catalogs, respectively. However, we cannot identify counterparts of the remaining 11 sources, F150DA-013, F150DA-047, F150DA-057, F150DB-004, F150DB-023, F150DB-056, F150DB-058, F200DB-015, F200DB-109, F200DB-175, and F200DB-181, probably because their SNRs are not sufficient to be identified in this study, the source is severely affected by nearby bright objects, or a WCS offset between Yan et al. (2023), and this study is too large to identify the counterparts. Among the 54 objects identified as F150W dropouts, F150DA-053 at $z = 11.71^{+1.56}_{-0.54}$ is SM-z12-1 at $z = 12.47^{+1.19}_{-0.72}$ in this study. We have checked the photometry of the other 53 and 11 objects identified in our original photometric catalogs, but none of them are selected as high-redshift candidates in this study, due to their insufficient colors of the break, $\Delta\chi^2 < 9$, and/or an insufficient S/N in the detection image.

3.6.9. Summary of the Comparisons

In summary, we have found that bright candidates reported in previous studies are reproduced in this study, such as GL-z9-1, GL-z12-1, CR2-z12-1, and CR2-z16-1. However, some of faint candidates reported in other studies are not selected in our selection criteria, because most of these faint candidates are selected by photometric redshifts but with a weak criterion (e.g., $\Delta\chi^2 > 4$) or by relatively weak color selection criteria (e.g., F150W – F200W > 0.5). It is expected that the contamination fraction in such faint candidates is high, given the small $\Delta\chi^2$ values (see discussions in Section 3.3). These comparisons indicate that our selection criteria are conservative enough to remove foreground interlopers while keeping bright and reliable candidates.

3.7. Contamination

We check whether our sample is largely contaminated by foreground interlopers or not. One of the major sources for contamination is related to low-redshift galaxies whose Balmer breaks are redshifted to the wavelength of the Lyman break of our dropout galaxies. To test the effect of such contamination, we make a mock catalog of galaxies with Balmer breaks at $z = 0-8$. We first generate model spectra of galaxies by using

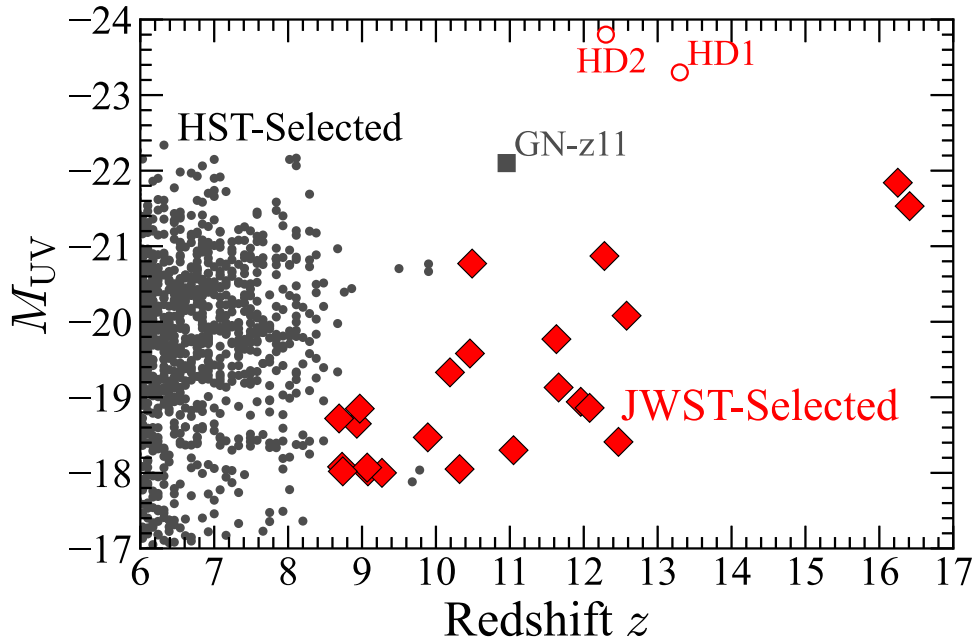


Figure 6. Absolute UV magnitude as a function of the redshift for galaxies at $6 < z < 16$. The red diamonds represent our dropout galaxy candidates selected with the JWST images. The red open circles show HD1 and HD2 previously found by the combination of the images taken with Spitzer and ground-based telescopes (Harikane et al. 2022a). The gray square and circles denote GN-z11 (Oesch et al. 2016; Jiang et al. 2021) and dropout galaxies selected with deep HST images (Bouwens et al. 2015).

PANHIT (Mawatari et al. 2020b) assuming a delayed- τ star formation history, $\tau = 0.01, 0.03, 0.1, 0.3,$ and 1 Gyr; stellar age of 0.01 – 1.3 Gyr; and metallicity of $Z = 0.0001, 0.0004, 0.004, 0.008, 0.02,$ and 0.05 . In Figure 10 we plot model tracks of the $z = 0$ – 8 galaxies with colors of our selected galaxy candidates and our color selection criteria. We find that the $z = 0$ – 8 galaxies with Balmer breaks have a relatively small break color (e.g., $F150W - F200W < 1.0$ in the F150W-dropout selection) or larger break color and red continuum color ($F150W - F200W > 1.0$ and $F200W - F356W > 0$). Our color selection criteria avoid model tracks of these $z = 0$ – 8 galaxies, and most of our candidates are located far from these model tracks. In the right panel of Figure 10, we also plot a dusty starburst galaxy at $z \sim 5$, which may appear as a $z > 15$ galaxy discussed in Zavala et al. (2023). Such a dusty interloper is also removed from our sample due to the red continuum color ($F277W - F444W > 1.0$).

To evaluate the effect of contamination from low-redshift objects scattering into our selection criteria due to the photometric noise at the depth of the observations, we conduct Monte Carlo simulations using the real data sets in the same manner as previous studies (e.g., Bouwens et al. 2015; Ono et al. 2018; Harikane et al. 2022b). We start from multiband catalogs constructed in the GLASS field whose images are sufficiently deep. We create 100 mock catalogs by perturbing the measured fluxes by adding photometric scatters based on the flux uncertainties in each band in the CEERS and Stephan’s Quintet fields whose depths are shallower than the GLASS field. We select high-redshift galaxies from the mock catalogs with the same selection criteria as our real selection. In the same manner as Bouwens et al. (2015), we classify sources that are selected but that show detections in the band that is bluer than the break in the original catalogs as contaminants. Based on these simulations, we find that the contamination rate due to the scatter is $< 6\%$ for the F150W-

and F200W-dropout selections. The contamination rates for the F115W-dropout selection cannot be evaluated with this procedure, because the galaxy selection is conducted only in the GLASS field where we start the simulation. However, the good agreement in the $z \sim 9$ number densities between our results and previous studies (Section 5.2) indicates that the contamination is not significant in our F115W-dropout sample.

To further test the contamination, we stack images of the 13 F115W-dropout candidates and 8 F150W-dropout candidates. If the sample is significantly contaminated by low-redshift interlopers, the stacked images should show signals in a band whose wavelength is bluer than the Lyman break. Figure 11 presents stacked images of our F115W- and F150W-dropout candidates. There are no significant positive signals found in the F090W band and in the F090W and F115W bands for the F115W- and F150W-dropout candidates, respectively, suggesting that our samples are not significantly contaminated by low-redshift interlopers. These tests and comparisons in Section 3.6 indicate that our conservative selection criteria with careful screening of low-redshift interlopers provide a reliable sample of $z \sim 9$ – 16 galaxy candidates, suitable for statistical studies such as luminosity function measurements.

4. Mass Model

Various mass models for SMACS J0723 are produced by parametric mass modeling algorithms. The RELICS survey (Coe et al. 2019) team provides the mass models¹³ developed with the LENSTOOL (Jullo et al. 2007; Fox et al. 2022) and GLAFIC (Oguri 2010) codes, both of which are constructed using HST data. A new model with the Lenstool code is

¹³ <https://archive.stsci.edu/prepds/relics/>

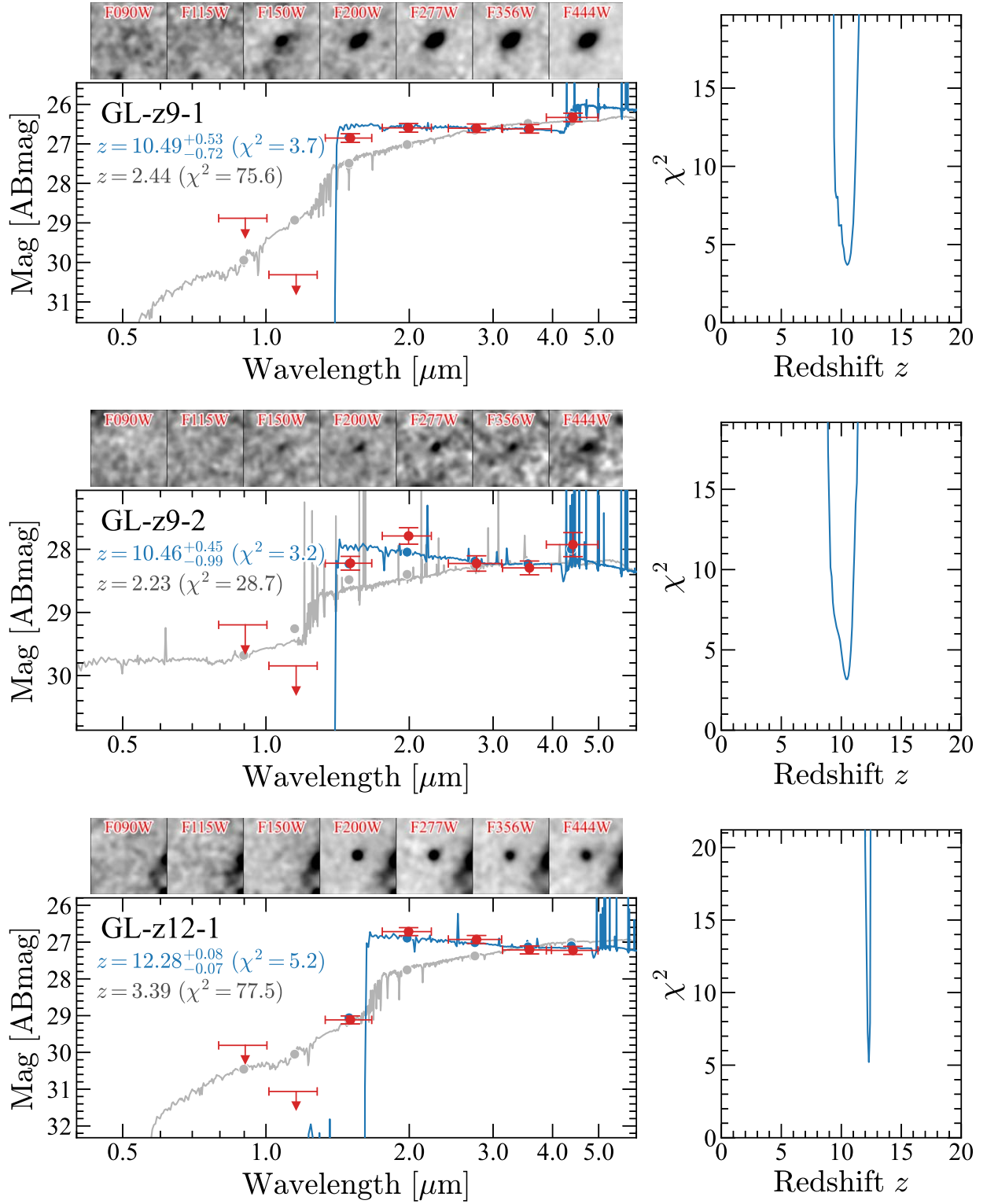


Figure 7. (Top) The left panel presents the optical to near-infrared SEDs of the $z \sim 9$ dropout galaxy, GL-z9-1. The red circles and arrows show the measured magnitudes and 2σ upper limits, respectively. The blue curve denotes the best-fit model SED whose redshift and 2σ errors are presented in the upper left with the blue labels. The gray curve is a significantly worse fit of a low-redshift solution. The images on this panel are $1''.5 \times 1''.5$ cutout images of GL-z9-1 in the NIRCcam bands with a 3 pixel smoothing whose band names are indicated with the red labels. The right panel shows χ^2 values of the SED fitting as a function of the redshift. (Middle) Same as the top panels, but for another $z \sim 9$ dropout galaxy candidate, GL-z9-2. (Bottom) Same as the top panels, but for a $z \sim 12$ dropout galaxy candidate, GL-z12-1.

constructed with JWST ERO data in Mahler et al. (2022). Golubchik et al. (2022) recently presented a mass model of SMACS J0723 developed by the light-traces-mass (LTM; Broadhurst et al. 2005; Zitrin et al. 2009, 2015) approach

before the JWST ERO data release, and subsequently Pascale et al. (2022) presented LTM modeling with the JWST ERO data. Caminha et al. (2022) also developed the mass model of SMACS J0723 using LENSTOOL.

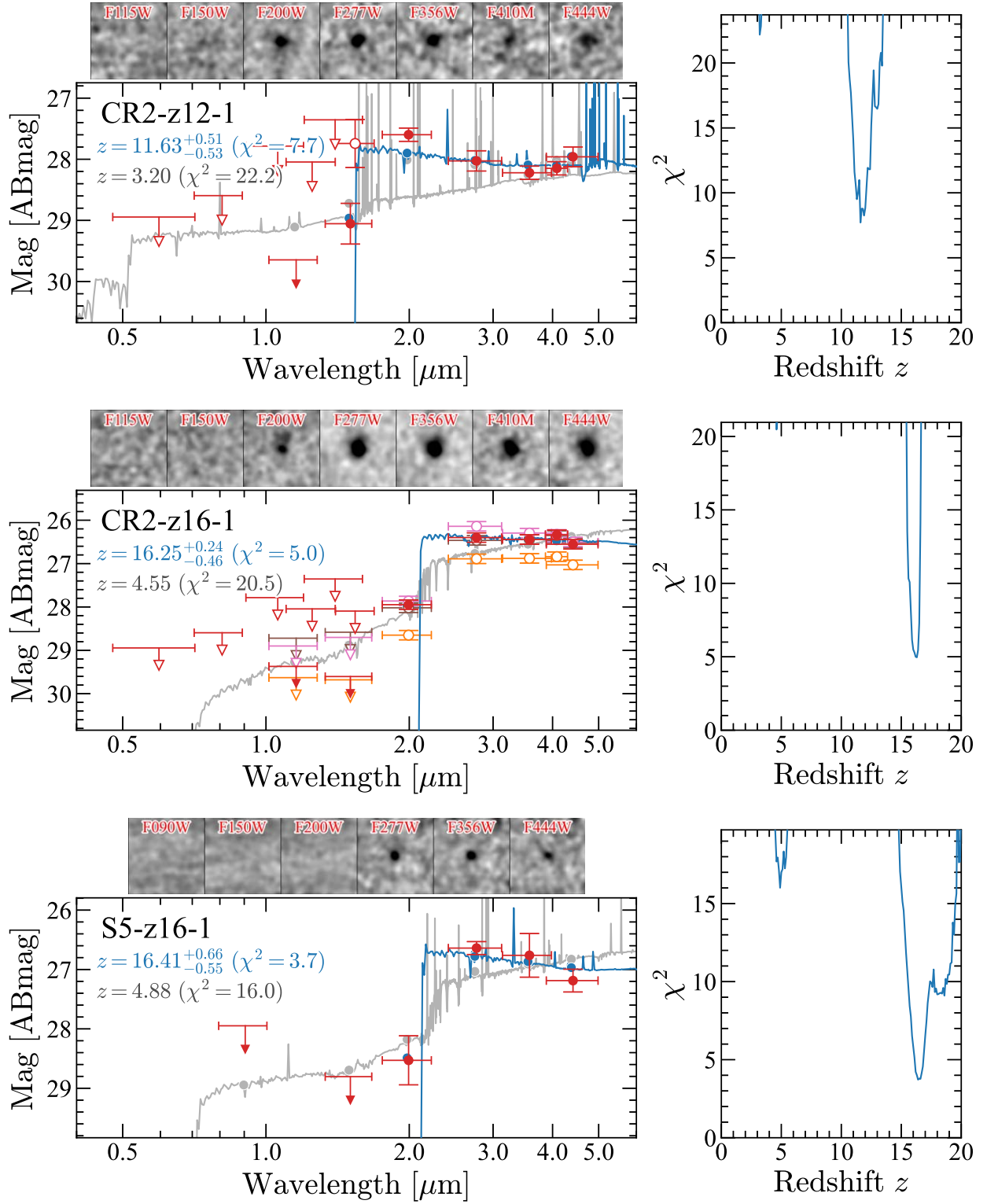


Figure 8. Same as Figure 7, but for a $z \sim 12$ dropout galaxy candidate, CR2-z12-1 (top), and $z \sim 16$ dropout galaxy candidates, CR2-z16-1 (middle) and S5-z16-1 (bottom). The open red symbols denote the measurements and the limits obtained with HST/ACS and WFC3. The orange, pink, and brown open symbols in the middle panel are measurements in Donnan et al. (2023), Naidu et al. (2022a), and Finkelstein et al. (2022c), respectively.

In this paper, we construct an updated GLAFIC (Oguri 2010, 2021) strong lens mass model of SMACS0723 using the new JWST ERO data. The magnification factors predicted by the updated GLAFIC mass model are compared with those from the other existing mass models to evaluate the

lens-model uncertainty. The GLAFIC code performs the so-called parametric lens mass modeling, where shapes of the mass distributions of the cluster are described by a superposition of a small number of lens mass components with known profile shapes, and parameters characterizing the lens

Table 3
Summary of Our F115W-dropout Candidates at $z \sim 9$

ID (1)	R.A. (2)	Decl. (3)	F356W (4)	F115W – F150W (5)	F150W – F277W (6)	M_{UV} (7)	z_{phot} (8)	$\Delta\chi^2$ (9)	References/Note (10)
GLASS									
GL-z9-1	00:14:02.85	-30:22:18.6	26.6 ± 0.1	>4.1	0.2 ± 0.1	-20.9 ± 0.1	$10.49^{+0.53}_{-0.72}$	71.9	This,N22,C22,D22
GL-z9-2	00:14:03.28	-30:21:05.6	28.3 ± 0.1	>2.3	-0.0 ± 0.1	-19.7 ± 0.1	$10.46^{+0.45}_{-0.99}$	25.5	This,C22
GL-z9-3	00:14:00.09	-30:19:06.9	28.4 ± 0.1	1.7 ± 0.5	-0.4 ± 0.2	-18.8 ± 0.1	$8.93^{+0.39}_{-0.38}$	22.6	This
GL-z9-4	00:14:00.27	-30:21:25.9	28.5 ± 0.1	>2.5	0.2 ± 0.1	-19.4 ± 0.1	$10.19^{+0.63}_{-0.55}$	27.2	This,D22
GL-z9-5	00:14:03.10	-30:22:26.3	28.7 ± 0.1	1.3 ± 0.3	-0.6 ± 0.2	-18.8 ± 0.1	$8.69^{+0.42}_{-0.15}$	10.3	This
GL-z9-6	00:14:04.37	-30:20:39.6	28.7 ± 0.1	1.2 ± 0.3	-0.0 ± 0.1	-18.9 ± 0.1	$8.97^{+0.36}_{-0.36}$	13.0	This
GL-z9-7	00:14:02.52	-30:21:57.0	28.9 ± 0.1	>2.0	0.7 ± 0.1	-18.2 ± 0.2	$10.32^{+0.74}_{-0.82}$	12.0	This
GL-z9-8	00:14:00.83	-30:21:29.8	29.1 ± 0.1	1.9 ± 0.5	-0.7 ± 0.2	-18.1 ± 0.2	$9.08^{+0.94}_{-0.32}$	31.2	This
GL-z9-9	00:14:03.71	-30:21:03.6	29.1 ± 0.1	>2.1	-0.1 ± 0.2	-18.1 ± 0.2	$9.27^{+1.28}_{-0.61}$	20.5	This
GL-z9-10	00:14:03.47	-30:19:00.9	29.1 ± 0.1	1.2 ± 0.4	-0.2 ± 0.2	-18.2 ± 0.2	$8.73^{+0.68}_{-0.41}$	22.0	This
GL-z9-11	00:14:02.49	-30:22:00.9	29.4 ± 0.1	1.9 ± 0.5	-0.8 ± 0.2	-18.6 ± 0.1	$9.89^{+0.21}_{-0.74}$	41.0	This
GL-z9-12	00:14:06.85	-30:22:02.0	29.7 ± 0.1	1.3 ± 0.5	-0.7 ± 0.3	-18.2 ± 0.2	$9.07^{+1.02}_{-0.23}$	50.9	This
GL-z9-13	00:13:57.45	-30:18:00.0	29.7 ± 0.1	1.1 ± 0.3	-0.8 ± 0.2	-18.1 ± 0.3	$8.74^{+0.57}_{-0.28}$	110.3	This
Other Possible Candidates that did not Meet Our Selection Criteria									
Castellano et al. (2022)									
GHZ3	00:14:06.94	-30:21:49.7	27.0 ± 0.1	>2.8	0.7 ± 0.1	-19.7 ± 0.1	$11.02^{+0.37}_{-0.47}$	8.6	2
GHZ5	00:13:58.66	-30:18:27.4	28.8 ± 0.1	1.1 ± 0.4	-0.2 ± 0.2	-18.8 ± 0.2	$8.50^{+0.86}_{-1.86}$	22.3	1
GHZ6	00:13:54.97	-30:18:53.7	27.8 ± 0.1	1.3 ± 0.6	0.8 ± 0.1	-18.8 ± 0.1	$2.20^{+8.99}_{-0.38}$	-2.8	2

Note. (1) Name. (2) R.A. (3) Decl. (4) Total magnitude in the F356W band with 1σ errors. (5) F115W – F150W color with 1σ errors. (6) F150W – F277W color with 1σ errors. (7) Absolute UV magnitude with 1σ errors. (8) Photometric redshift with 2σ errors. (9) χ^2 difference between the best high-redshift solution and a lower-redshift solution, $\Delta\chi^2 = \chi^2(z_{\text{low}}) - \chi^2(z_{\text{high}})$. (10) Reference (This: this work; N22: Naidu et al. 2022b; C22: Castellano et al. 2022; D22: Donnan et al. 2023) and note for a reason why the source is not selected in this study (1: $>2\sigma$ detection in F090W, 2: $\Delta\chi^2 < 9.0$).

mass components are determined so as to reproduce observed positions of multiple images.

As a specific procedure, we largely follow the methodology described in Kawamata et al. (2016). We model the dark matter halo by an elliptical Navarro–Frenk–White (NFW; Navarro et al. 1997) density profile with an approximation to speed up the calculation of its lensing property (see Oguri 2021). The model parameters associated with the NFW component are the mass, the center, the ellipticity and its position angle, and the concentration parameter. In addition to the main NFW halo, we place an additional NFW component whose center is fixed to a bright cluster member galaxy located northwest, (R.A., decl.) = (110.7928634, -73.4476417). We also fix the concentration parameter of the additional NFW component to $c = 10$, and fit its mass, ellipticity, and position angle only. Cluster member galaxies selected by photometric redshifts from the RELICS HST data (Coe et al. 2019) are modeled by an elliptical pseudo Jaffe profile. In order to reduce the number of parameters, the velocity dispersion σ and the truncation radius r_{trunc} of each cluster member galaxy are assumed to scale with its luminosity (in the HST F814W band) as $\sigma \propto L^{1/4}$ and $r_{\text{trunc}} \propto L^\eta$, with their normalization and η being treated as free parameters. In addition we include an external shear to improve the fitting. For multiple image sets without spectroscopic redshifts, we simultaneously fit their redshifts.

We search for the best-fitting model by the standard χ^2 minimization, where χ^2 is computed from the differences between observed and model-predicted positions. We assume the positional error of $0''.4$, which is a typical positional accuracy achieved by the parametric strong lens mass modeling (Kawamata et al. 2016). The χ^2 is evaluated in the source plane, taking account of the full magnification tensor at each multiple image position (see Appendix 2 of Oguri 2010). Errors

on the model parameters are derived using the standard MCMC technique. Multiple images are identified iteratively, starting with secure sets of multiple images that are obvious from their colors, morphologies, and redshifts, constructing a preliminary mass model with those sets of multiple images, and searching for new multiple sets with the help of the preliminary mass model. In this work, we use 12 sets of multiple images for our strong lens mass modeling, with a total number of multiple images of 38. These multiple image sets are mostly consistent with other work using different lens modeling codes (Mahler et al. 2022; Pascale et al. 2022). We adopt spectroscopic redshifts for five sets of multiple images given in the literature (Golubchik et al. 2022; Mahler et al. 2022; Pascale et al. 2022). Our best-fitting model has $\chi^2 = 28.3$ for a degree of freedom of 32, representing a good fit. The rms of differences between observed and predicted multiple image positions is $0''.35$.

With the updated GLAFIC mass model, we calculate the magnification factors μ of our dropout galaxy candidates and the effective survey volume. Table 6 summarizes the magnification factors of our dropout galaxy candidate and spectroscopically confirmed galaxies at $z > 7$ calculated by GLAFIC, Mahler et al. (2022), Pascale et al. (2022), and Caminha et al. (2022). We find that the magnification factors calculated by each model are in good agreement, typically within $\sim 20\%$.

5. Luminosity Function

5.1. Sample Completeness

To derive the rest-frame UV luminosity function, we estimate the completeness of our dropout galaxy selection in the same manner as previous studies (e.g., Ouchi et al. 2009; Ono et al. 2018; Harikane et al. 2022b). We conduct Monte

Table 4
Summary of Our F150W-dropout Candidates at $z \sim 12$

ID (1)	R.A. (2)	Decl. (3)	F356W (4)	F150W – F200W (5)	F200W – F356W (6)	M_{UV} (7)	z_{phot} (8)	$\Delta\chi^2$ (9)	References/ Note (10)
SMACS J0723									
SM-z12-1	07:22:32.59	-73:28:33.3	29.8 ± 0.6	1.9 ± 0.9	-1.2 ± 0.6	-18.5 ± 0.1	$12.47^{+1.19}_{-0.72}$	14.5	This, Y22
GLASS									
GL-z12-1	00:13:59.74	-30:19:29.1	27.2 ± 0.1	2.4 ± 0.1	-0.5 ± 0.1	-21.0 ± 0.1	$12.28^{+0.08}_{-0.07}$	72.3	This, N22, C22, D22
CEERS2									
CR2-z12-1	14:19:46.36	+52:56:32.8	28.2 ± 0.1	1.5 ± 0.4	-0.6 ± 0.1	-19.9 ± 0.1	$11.63^{+0.51}_{-0.53}$	14.5	This, F22, D22
CR2-z12-2	14:19:42.57	+52:54:42.0	28.6 ± 0.1	1.3 ± 0.6	-0.1 ± 0.1	-19.0 ± 0.2	$11.96^{+1.44}_{-0.87}$	14.0	This
CR2-z12-3	14:19:41.61	+52:55:07.6	28.8 ± 0.1	1.4 ± 0.5	-0.6 ± 0.1	-19.2 ± 0.2	$11.66^{+0.69}_{-0.71}$	20.3	This
CR2-z12-4	14:19:24.86	+52:53:13.9	28.9 ± 0.1	1.6 ± 1.1	0.1 ± 0.2	-19.0 ± 0.2	$12.08^{+2.11}_{-1.25}$	9.1	This
CEERS3									
CR3-z12-1	14:19:11.11	+52:49:33.6	29.8 ± 0.2	1.0 ± 0.7	-0.5 ± 0.2	-18.4 ± 0.4	$11.05^{+2.24}_{-0.47}$	47.1	This
Stephan's Quintet									
S5-z12-1	22:36:06.72	+34:00:09.7	27.9 ± 0.5	>2.3	-0.2 ± 0.5	-20.2 ± 0.1	$12.58^{+1.23}_{-0.46}$	19.1	This
Other Possible Candidates that did not Meet Our Selection Criteria									
Adams et al. (2023)									
10234	07:22:39.60	-73:30:06.2	29.8 ± 0.6	0.5 ± 0.4	-0.7 ± 0.6	-18.3 ± 0.1	$5.34^{+0.30}_{-0.04}$	-75.2	1,2,3
Atek et al. (2023)									
SMACS_z12a	07:22:47.38	-73:30:01.7	28.0 ± 0.3	0.7 ± 0.5	0.2 ± 0.3	-18.5 ± 0.1	$3.15^{+1.15}_{-1.60}$	-36.4	2,3
SMACS_z12b	07:22:52.26	-73:27:55.4	28.4 ± 0.2	1.5 ± 0.6	-0.1 ± 0.2	-18.4 ± 0.1	$3.03^{+0.29}_{-1.48}$	-5.4	3
Donnan et al. (2023)									
10566	07:23:03.55	-73:28:46.8	29.0 ± 0.4	1.3 ± 0.2	-1.6 ± 0.4	-19.0 ± 0.1	$1.87^{+9.73}_{-0.17}$	-3.2	3
1566	07:22:39.31	-73:30:00.6	28.8 ± 0.3	1.9 ± 1.1	-0.4 ± 0.4	-18.1 ± 0.1	$12.15^{+1.54}_{-1.24}$	4.8	3
27535_4	14:19:27.31	+52:51:29.2	27.6 ± 0.1	>1.8	-0.1 ± 0.1	-19.0 ± 0.2	$3.90^{+0.29}_{-0.06}$	-7.1	3
Yan et al. (2023)									
F150DB-007	07:23:23.97	-73:27:58.7	28.0 ± 0.3	0.4 ± 0.4	0.4 ± 0.4	-18.5 ± 0.1	$4.79^{+0.45}_{-0.80}$	-101.7	2,3
F150DB-011	07:23:27.39	-73:27:58.0	29.1 ± 0.7	0.1 ± 0.1	-1.5 ± 0.7	-17.9 ± 0.1	$2.57^{+0.02}_{-0.02}$	-110.2	2,3
F150DB-013	07:23:05.53	-73:27:50.6	28.6 ± 0.4	1.2 ± 0.4	-1.0 ± 0.4	-18.7 ± 0.1	$2.97^{+0.17}_{-0.18}$	-69.6	3
F150DB-021	07:23:12.64	-73:27:45.2	27.1 ± 0.1	0.1 ± 0.1	0.2 ± 0.1	-18.8 ± 0.1	$2.43^{+4.22}_{-0.93}$	-37.7	2,3
F150DB-026	07:23:23.74	-73:27:40.6	29.6 ± 0.6	0.1 ± 0.3	-0.4 ± 0.6	-16.5 ± 0.3	$10.38^{+1.08}_{-1.26}$	18.1	2
F150DB-031	07:23:21.43	-73:27:36.3	28.8 ± 0.4	1.1 ± 0.5	-0.4 ± 0.4	-16.6 ± 0.3	$11.59^{+0.90}_{-9.48}$	3.9	3
F150DB-033	07:23:30.55	-73:27:33.1	27.2 ± 0.1	0.8 ± 0.2	0.5 ± 0.1	-18.3 ± 0.1	$11.38^{+0.42}_{-0.58}$	4.4	2,3
F150DB-040	07:23:11.94	-73:27:24.9	29.1 ± 0.3	-0.2 ± 0.3	0.1 ± 0.4	-15.7 ± 0.6	$4.74^{+0.15}_{-0.62}$	-87.3	2,3
F150DB-041	07:23:06.63	-73:27:25.4	27.3 ± 0.1	0.2 ± 0.2	0.4 ± 0.2	-17.9 ± 0.1	$1.69^{+0.19}_{-1.01}$	-49.9	2,3
F150DB-044	07:23:39.31	-73:27:22.3	28.8 ± 0.4	0.7 ± 0.3	-0.7 ± 0.4	-18.5 ± 0.1	$3.45^{+0.36}_{-0.27}$	-99.8	2,3
F150DB-048	07:23:01.57	-73:27:18.0	27.6 ± 0.1	1.3 ± 0.7	0.8 ± 0.2	-17.8 ± 0.1	$12.39^{+2.69}_{-10.33}$	0.8	3
F150DB-050	07:23:24.58	-73:27:15.0	29.0 ± 0.4	0.1 ± 0.2	-0.6 ± 0.4	-16.6 ± 0.3	$3.00^{+0.07}_{-0.79}$	-109.3	2,3
F150DB-052	07:23:28.14	-73:27:13.8	29.2 ± 0.5	0.5 ± 0.5	-0.2 ± 0.5	-15.7 ± 0.7	$3.75^{+1.09}_{-0.32}$	-68.0	2,3
F150DB-054	07:23:12.51	-73:27:10.7	29.6 ± 0.6	0.0 ± 0.5	-0.1 ± 0.7	-16.0 ± 0.4	$4.60^{+0.63}_{-0.75}$	-55.9	2,3
F150DB-069	07:23:04.26	-73:26:54.2	29.4 ± 0.5	1.1 ± 0.5	-1.0 ± 0.5	-17.5 ± 0.1	$11.99^{+1.47}_{-0.81}$	33.8	4
F150DB-075	07:23:02.23	-73:26:41.5	27.1 ± 0.1	0.8 ± 0.1	-0.3 ± 0.1	-19.8 ± 0.1	$2.87^{+0.10}_{-1.55}$	-45.8	2,3
F150DB-076	07:23:29.41	-73:26:39.7	28.6 ± 0.4	0.4 ± 0.2	-0.6 ± 0.5	-18.2 ± 0.1	$3.78^{+0.04}_{-0.03}$	-100.7	2,3
F150DB-079	07:23:13.15	-73:26:29.6	28.9 ± 0.4	0.9 ± 0.4	-0.5 ± 0.4	-18.1 ± 0.1	$2.75^{+0.40}_{-0.08}$	-32.2	2,3
F150DB-082	07:23:22.75	-73:26:25.6	27.9 ± 0.2	1.2 ± 0.6	0.1 ± 0.3	-18.5 ± 0.1	$3.05^{+0.36}_{-1.86}$	-13.5	3
F150DB-084	07:23:07.54	-73:26:23.8	29.2 ± 0.4	0.2 ± 0.3	-0.6 ± 0.5	-18.8 ± 0.1	$3.00^{+0.00}_{-0.27}$	-14.3	2,3
F150DB-088	07:23:14.04	-73:26:17.3	26.3 ± 0.1	1.2 ± 0.3	0.2 ± 0.1	-19.6 ± 0.1	$3.06^{+0.48}_{-0.32}$	-41.2	3
F150DB-090	07:23:26.23	-73:26:13.8	25.7 ± 0.1	0.8 ± 0.1	0.6 ± 0.1	-20.6 ± 0.1	$3.19^{+0.87}_{-0.20}$	-93.5	2,3
F150DB-095	07:23:24.76	-73:26:01.2	28.3 ± 0.3	0.2 ± 0.2	-0.5 ± 0.3	-19.1 ± 0.1	$2.85^{+0.43}_{-0.14}$	-113.6	2,3
F150DB-C_4	07:23:25.96	-73:26:39.9	23.2 ± 0.1	2.0 ± 0.3	2.7 ± 0.1	-21.4 ± 0.1	$5.28^{+0.16}_{-0.12}$	-94.0	3
F150DA-005	07:22:41.01	-73:29:54.9	27.9 ± 0.2	0.4 ± 0.2	-0.3 ± 0.2	-19.8 ± 0.1	$3.01^{+1.09}_{-0.24}$	-113.8	2,3
F150DA-007	07:22:44.88	-73:29:53.6	28.5 ± 0.2	0.3 ± 0.3	0.1 ± 0.2	-19.3 ± 0.1	$10.99^{+0.74}_{-0.56}$	7.9	2,3
F150DA-008	07:22:52.75	-73:29:51.6	28.1 ± 0.3	0.7 ± 0.3	-0.2 ± 0.3	-19.6 ± 0.1	$2.99^{+0.30}_{-1.91}$	-49.2	2,3
F150DA-010	07:22:40.09	-73:29:46.1	28.5 ± 0.4	0.3 ± 0.3	-0.4 ± 0.4	-19.1 ± 0.1	$3.54^{+0.98}_{-1.92}$	-79.9	2,3
F150DA-015	07:22:44.74	-73:29:26.8	28.0 ± 0.2	0.7 ± 0.3	0.1 ± 0.2	-19.6 ± 0.1	$3.01^{+1.63}_{-0.24}$	-106.8	2,3
F150DA-018	07:22:56.02	-73:29:21.9	29.0 ± 0.3	1.6 ± 0.8	-0.5 ± 0.4	-18.7 ± 0.1	$12.84^{+0.97}_{-1.27}$	19.1	4
F150DA-019	07:22:39.40	-73:29:20.5	28.7 ± 0.3	0.5 ± 0.3	-0.3 ± 0.3	-19.5 ± 0.1	$2.23^{+9.39}_{-0.22}$	-2.8	2,3
F150DA-020	07:22:55.87	-73:29:17.4	28.3 ± 0.2	0.9 ± 0.3	-0.1 ± 0.2	-19.5 ± 0.1	$3.50^{+0.68}_{-0.22}$	-98.4	2,3

Table 4
(Continued)

ID (1)	R.A. (2)	Decl. (3)	F356W (4)	F150W – F200W (5)	F200W – F356W (6)	M_{UV} (7)	z_{phot} (8)	$\Delta\chi^2$ (9)	References/ Note (10)
F150DA-024	07:22:33.46	-73:29:09.5	28.8 ± 0.3	0.5 ± 0.2	-0.7 ± 0.3	-18.8 ± 0.1	2.62 ^{+0.06} _{-0.06}	-77.3	2,3
F150DA-026	07:22:46.02	-73:29:08.1	30.6 ± 1.2	0.0 ± 0.6	< -0.7	-18.9 ± 0.1	4.58 ^{+0.64} _{-0.35}	-60.9	2,3
F150DA-027	07:23:01.03	-73:29:07.1	20.0 ± 0.1	0.1 ± 0.1	-0.9 ± 0.1	-27.1 ± 0.1	3.47 ^{+0.07} _{-3.21}	-109.0	2,3
F150DA-031	07:22:40.65	-73:29:00.5	28.4 ± 0.2	1.1 ± 0.6	-0.0 ± 0.3	-19.3 ± 0.1	11.95 ^{+2.69} _{-9.28}	3.9	3
F150DA-038	07:23:02.95	-73:28:46.1	29.0 ± 0.4	0.7 ± 0.4	-0.6 ± 0.5	-18.8 ± 0.1	2.74 ^{+9.09} _{-0.89}	-2.7	2,3
F150DA-039	07:23:00.58	-73:28:47.0	28.3 ± 0.3	0.5 ± 0.3	-0.3 ± 0.3	-18.8 ± 0.1	3.02 ^{+0.28} _{-1.29}	-45.2	2,3
F150DA-050	07:22:45.00	-73:28:36.9	28.1 ± 0.2	-0.2 ± 0.2	-0.2 ± 0.2	-19.1 ± 0.1	1.94 ^{+0.40} _{-0.19}	-78.1	2,3
F150DA-052	07:22:26.94	-73:28:33.8	28.2 ± 0.2	0.7 ± 0.5	0.2 ± 0.3	-19.2 ± 0.1	1.58 ^{+1.95} _{-0.25}	-13.2	2,3
F150DA-054	07:22:38.89	-73:28:30.8	28.8 ± 0.3	0.7 ± 0.3	-0.3 ± 0.3	-19.2 ± 0.1	3.04 ^{+0.31} _{-0.33}	-105.0	2,3
F150DA-058	07:22:48.28	-73:28:27.3	27.8 ± 0.2	0.6 ± 0.2	-0.1 ± 0.2	-19.5 ± 0.1	2.96 ^{+0.32} _{-1.88}	-71.1	2,3
F150DA-060	07:22:40.75	-73:28:23.7	28.6 ± 0.3	0.5 ± 0.4	0.0 ± 0.3	-18.9 ± 0.1	3.74 ^{+0.69} _{-1.53}	-70.3	2,3
F150DA-062	07:22:54.22	-73:28:23.5	28.6 ± 0.2	0.4 ± 0.2	-0.2 ± 0.2	-19.3 ± 0.1	1.80 ^{+9.47} _{-0.14}	-1.1	2,3
F150DA-063	07:22:53.83	-73:28:23.2	27.1 ± 0.1	0.0 ± 0.1	-0.0 ± 0.1	-19.9 ± 0.1	6.99 ^{+0.02} _{-5.26}	1.6	2,3
F150DA-066	07:22:39.61	-73:28:12.1	29.1 ± 0.3	0.8 ± 0.2	-1.3 ± 0.4	-19.3 ± 0.1	2.99 ^{+0.06} _{-0.19}	-118.6	2,3
F150DA-075	07:22:38.35	-73:27:57.1	28.1 ± 0.2	0.5 ± 0.2	-0.1 ± 0.2	-19.1 ± 0.1	3.27 ^{+0.58} _{-0.91}	-59.3	2,3
F150DA-077	07:22:52.23	-73:27:55.4	28.4 ± 0.2	1.5 ± 0.6	-0.1 ± 0.2	-19.0 ± 0.1	1.45 ^{+1.37} _{-0.06}	-4.6	3
F150DA-078	07:22:49.24	-73:27:49.8	28.1 ± 0.2	0.1 ± 0.2	0.1 ± 0.2	-19.3 ± 0.1	1.94 ^{+0.32} _{-0.78}	-16.8	2,3
F150DA-081	07:22:49.24	-73:27:44.5	27.9 ± 0.2	0.3 ± 0.3	0.3 ± 0.2	-19.1 ± 0.1	1.43 ^{+1.47} _{-0.09}	-16.9	2,3
F150DA-082	07:22:52.78	-73:27:41.9	29.2 ± 0.4	1.1 ± 0.4	-0.9 ± 0.4	-18.3 ± 0.1	2.58 ^{+0.03} _{-0.02}	-78.6	3
F150DA-083	07:22:42.72	-73:27:32.3	28.8 ± 0.3	0.2 ± 0.3	-0.3 ± 0.3	-19.3 ± 0.1	4.38 ^{+0.34} _{-0.09}	-72.1	2,3

Note. (1) Name. (2) R.A. (3) Decl. (4) Total magnitude in the F356W band with 1σ errors. (5) F150W – F200W color with 1σ errors. (6) F200W – F356W color with 1σ errors. (7) Absolute UV magnitude with 1σ errors. Values of galaxies in the SMACS J0723 field are after the lensing magnification correction with GLAFIC. (8) Photometric redshift with 2σ errors. (9) χ^2 difference between the best high-redshift solution and a lower-redshift solution, $\Delta\chi^2 = \chi^2(z_{\text{low}}) - \chi^2(z_{\text{high}})$. (10) Reference (This: this work; N22: Naidu et al. 2022b; C22: Castellano et al. 2022; D22: Donnan et al. 2023; F22: Finkelstein et al. 2022b; Y22: Yan et al. 2023) and note for a reason not selected in this study (1: $>2\sigma$ detection in F090W, 2: F150W – F200W < 1.0, 3: $\Delta\chi^2 < 9.0$, 4: $<5\sigma$ in the detection image).

Carlo simulations with real NIRCcam images and artificial galaxies mocking high-redshift galaxies. The mock high-redshift galaxies follow the size- M_{UV} redshift distribution revealed with the HST legacy data sets for galaxies at $z \sim 0-10$ (Shibuya et al. 2015), which is extrapolated to our redshift ranges, where the size- M_{UV} distribution is a log-normal distribution. Our initial measurements of sizes for our $z > 9$ galaxy candidates are consistent with this assumption within the uncertainties. We adopt the Sérsic index $n = 1$ found in typical galaxies at $z \sim 5-10$ (Ono et al. 2013; Shibuya et al. 2015) and the flat distribution of the intrinsic ellipticity in the range of 0.0–0.8. Recent studies indicate that morphologies of $z \sim 9-16$ galaxies identified in the JWST data sets are consistent with these assumptions (e.g., Ono et al. 2022). The SEDs of the mock high-redshift galaxies are uniformly distributed over magnitude and redshift, and have a color distribution agreeing with the $M_{UV}-\beta_{UV}$ relation observationally determined at $z \sim 8$ (Bouwens et al. 2014), where β_{UV} is the UV spectral slope index. The IGM absorption of Inoue et al. (2014) is applied to the SEDs, which produces absorption features in the wavelengths shorter than the Ly α line. We produce 100 artificial objects of the mock high-redshift galaxies with IRAF mkobject in each redshift and magnitude bin, and place the artificial objects on the real JWST NIRCcam images. With the images, we perform the object detection, photometry, color selection, and SED fitting in the same manner as Section 3. In the SMACS J0723 field, we consider the source magnification and multiple lensed images by using the mass model made with GLAFIC described in Section 4. Finally we calculate the selection completeness as a function of

the magnitude and redshift, $C(m, z)$, with the photometric catalogs of artificial high-redshift galaxies. Figure 9 presents examples of the selection completeness thus obtained. Although the average redshifts are $z = 10.1$ for F115W dropouts, $z = 13.8$ for F150W dropouts, and $z = 18.7$ for F200W dropouts, we use the median of the photometric redshifts of our selected candidates, $z = 9.1$ for F115W dropouts, $z = 12.0$ for F150W dropouts, and $z = 16.3$ for F200W dropouts, as the representative redshifts of each dropout sample.

Based on the results of these selection-completeness simulations, we estimate the survey volume per unit area as a function of the apparent magnitude (Steidel et al. 1999),

$$V_{\text{eff}}(m) = \int C(m, z) \frac{dV(z)}{dz} dz, \quad (10)$$

where $dV(z)/dz$ is the differential comoving volume as a function of the redshift. The space number density of our galaxy candidates that is corrected for incompleteness is calculated with the following equation:

$$\psi(m) = \frac{n(m)}{V_{\text{eff}}(m)}, \quad (11)$$

where $n(m)$ is the surface number density of selected galaxies in an apparent magnitude bin of m . We convert the number density as a function of the apparent magnitude, $\psi(m)$, into the UV luminosity functions, $\Phi[M_{UV}(m)]$, which are the number densities of galaxies as a function of the rest-frame UV absolute magnitude. Assuming a flat rest-frame UV continuum,

Table 5
Summary of Our F200W-dropout Candidates at $z \sim 16$

ID (1)	R.A. (2)	Decl. (3)	F356W (4)	F200W – F277W (5)	F277W – F444W (6)	M_{UV} (7)	z_{phot} (8)	$\Delta\chi^2$ (9)	References/ Note (10)
CEERS2									
CR2-z16-1	14:19:39.48	+52:56:34.9	26.4 ± 0.1	1.5 ± 0.1	-0.2 ± 0.1	-21.9 ± 0.1	$16.25^{+0.24}_{-0.46}$	15.5	This, D22
Stephan’s Quintet									
S5-z16-1	22:36:03.81	+33:54:16.7	26.8 ± 0.4	1.9 ± 0.5	-0.5 ± 0.2	-21.6 ± 0.3	$16.41^{+0.66}_{-0.55}$	12.3	This
Other Possible Candidates that did not Meet Our Selection Criteria									
Atek et al. (2023)									
SMACS_z16a	07:23:26.39	-73:28:04.5	28.0 ± 0.3	0.5 ± 0.1	-0.2 ± 0.1	-18.4 ± 0.8	$10.61^{+0.51}_{-8.55}$	-20.2	1,2
SMACS_z16b	07:22:39.57	-73:30:08.2	28.3 ± 0.2	0.7 ± 0.1	-0.3 ± 0.1	-19.3 ± 0.3	$15.15^{+0.50}_{-1.22}$	6.9	1,2
Yan et al. (2023)									
F200DB-045	07:23:22.77	-73:27:39.7	29.6 ± 0.6	0.1 ± 0.3	-0.3 ± 0.4	-16.9 ± 2.6	$4.39^{+1.73}_{-0.82}$	-9.8	1,2
F200DB-086	07:23:06.42	-73:27:19.8	29.9 ± 0.5	>1.4	0.4 ± 0.2	-16.8 ± 2.1	$17.13^{+2.87}_{-13.12}$	1.6	2
F200DB-159	07:23:25.35	-73:26:46.0	29.4 ± 0.6	-0.6 ± 0.2	-0.2 ± 0.3	-17.7 ± 1.1	$3.42^{+0.02}_{-0.23}$	-6.1	1,2
F200DA-006	07:22:40.35	-73:30:10.3	28.5 ± 0.3	0.2 ± 0.2	-0.7 ± 0.3	-19.7 ± 0.2	$10.50^{+0.73}_{-1.32}$	-10.8	1,2
F200DA-033	07:22:43.92	-73:29:15.7	25.8 ± 0.1	2.8 ± 0.3	1.4 ± 0.1	-22.5 ± 0.1	$5.75^{+0.40}_{-0.72}$	-7.0	2
F200DA-034	07:23:05.20	-73:29:13.4	28.7 ± 0.3	>1.5	-0.2 ± 0.3	-19.6 ± 0.3	$5.41^{+0.16}_{-0.01}$	-72.0	2
F200DA-040	07:23:03.93	-73:29:06.1	28.7 ± 0.3	0.3 ± 0.2	-0.3 ± 0.1	-19.2 ± 0.2	$3.94^{+0.97}_{-0.46}$	-102.5	1,2
F200DA-056	07:22:37.03	-73:28:41.5	29.2 ± 0.3	1.0 ± 0.3	-0.2 ± 0.1	-19.2 ± 0.2	$5.19^{+0.33}_{-0.35}$	-95.3	2
F200DA-061	07:22:31.69	-73:28:38.6	28.1 ± 0.2	0.5 ± 0.2	-0.2 ± 0.1	-19.6 ± 0.2	$4.91^{+0.70}_{-1.06}$	-97.1	1,2
F200DA-089	07:22:32.43	-73:28:06.8	28.1 ± 0.2	1.6 ± 0.9	0.7 ± 0.1	-19.8 ± 0.2	$15.73^{+4.21}_{-10.22}$	0.3	2
F200DA-098	07:22:34.80	-73:28:00.2	29.7 ± 0.9	>1.2	0.3 ± 0.3	-18.6 ± 0.7	$5.58^{+0.50}_{-0.70}$	-17.0	2

Note. (1) Name. (2) R.A. (3) Decl. (4) Total magnitude in the F356W band with 1σ errors. (5) F200W – F277W color with 1σ errors. (6) F277W – F444W color with 1σ errors. (7) Absolute UV magnitude with 1σ errors. Values of galaxies in the SMACS J0723 field are after the lensing magnification correction with GLAFIC. (8) Photometric redshift with 2σ errors. (9) χ^2 difference between the best high-redshift solution and a lower-redshift solution, $\Delta\chi^2 = \chi^2(z_{low}) - \chi^2(z_{high})$. (10) Reference (This: this work; D22: Donnan et al. 2023) and note for a reason not selected in this study (1: F200W – F277W < 1.0, 2: $\Delta\chi^2 < 9.0$).

we calculate the absolute UV magnitudes of galaxies from their apparent magnitudes in the bluest band not affected by the Lyman break, i.e., F200W, F277W, and F356W bands for F115W-, F150W-, and F200W-dropout galaxy candidates, respectively. The 1σ uncertainty is calculated by taking the Poisson confidence limit (Gehrels 1986) and cosmic variance into account. We estimate the cosmic variance in the number densities using the bias values of the $z \sim 7$ galaxies obtained in Harikane et al. (2016), following the procedures in Somerville et al. (2004).

5.2. Results

Figures 12 and 13 present our luminosity functions at $z \sim 9$, 12, and 16 together with luminosity functions obtained by previous work including the latest JWST studies (Bouwens et al. 2022b; Donnan et al. 2023; Finkelstein et al. 2022b; Naidu et al. 2022b). Our measurements of the luminosity functions are summarized in Table 7. Comparing with previous measurements of the luminosity functions, we find that our luminosity functions at $z \sim 9$ and 12 agree well with those of previous HST and JWST studies within the uncertainties, as shown in Figure 12. In Figure 13, we compare the luminosity function of our possible candidates at $z \sim 16$ newly determined by this study with those available at lower redshifts at $z \sim 14$ constrained by JWST. We confirm that these luminosity functions are comparable.

We conduct χ^2 minimization fitting of the double-power-law and Schechter functions to the luminosity functions that include the measurements at the bright end in the literature. In the

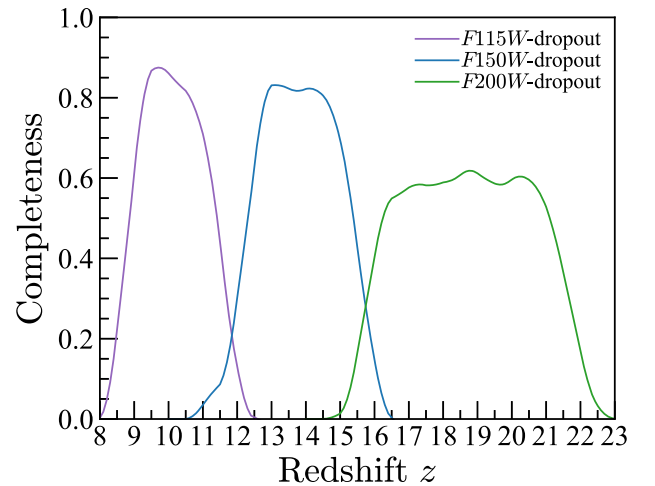


Figure 9. Selection completeness for our dropout galaxies. The purple, blue, and green curves show selection completeness for the F115W-, F150W-, and F200W-dropout galaxies whose rest-frame UV ($\sim 1500 \text{ \AA}$) magnitudes are F200W = 27.0 mag, F277W = 27.0 mag, and F356W = 27.0 mag, respectively. Each selection window is smoothed by $\Delta z = 1.0$.

fitting, we use the results of this study, Morishita et al. (2018), Bowler et al. (2020), and Bouwens et al. (2021) for the $z \sim 9$ luminosity function, the results of this study and Harikane et al. (2022a) for the $z \sim 12$ luminosity function assuming that the UV luminosity function does not rapidly change at $z \sim 12$ –13, and the result of this study for the $z \sim 16$ luminosity function. We show the best-fit functions in Figures 12 and 13, and

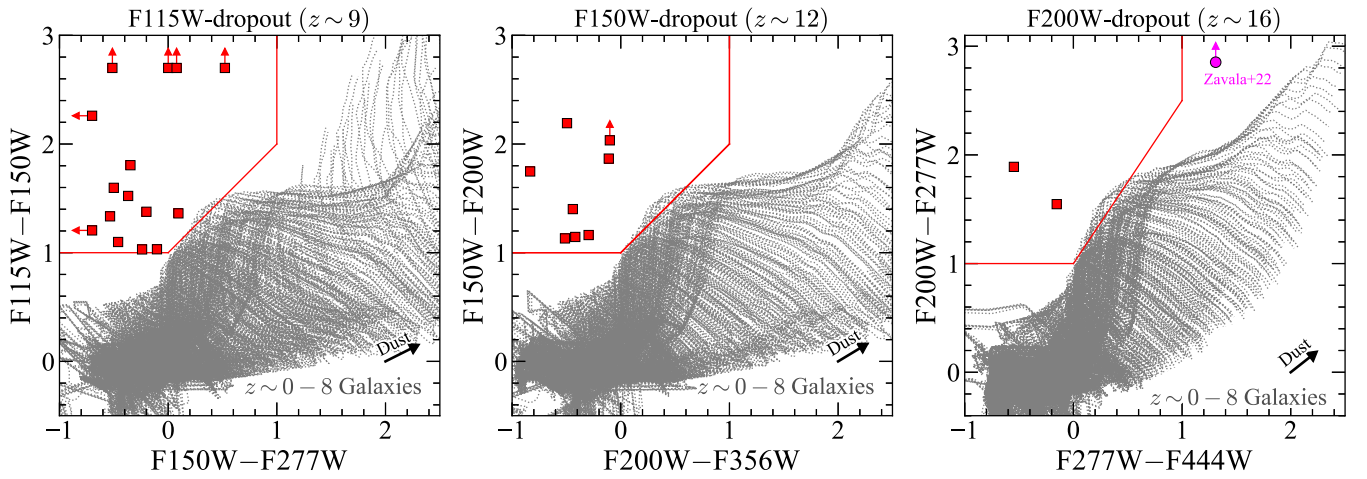


Figure 10. Same as Figure 2, but for evaluating the interlopers of foreground galaxies. The gray curves indicate colors of model galaxies at $z = 0-8$ that are produced with PANHIT (Mawatari et al. 2020b). See the text for details of the models. The black arrow indicates a shift of the colors with dust extinction of $\Delta E(B - V) = +0.1$. The magenta circle in the right panel is a dusty starburst galaxy at $z \sim 5$, which may appear as a $z > 15$ galaxy discussed in Zavala et al. (2023). Our color selection criteria avoid these low-redshift interlopers at $z \sim 0-8$.

present the best-fit parameters in Table 8. At $z \sim 9$, the χ^2 values of the fitting suggest that the double-power-law function explains the luminosity functions ($\chi^2/\text{dof} = 2.3/9$) better than the Schechter functions ($\chi^2/\text{dof} = 3.6/10$), albeit with a moderately small difference of χ^2 ($\sim 1\sigma$). At $z \sim 12$ and 16, we find no significant differences between the double-power-law and Schechter functions in the χ^2 values, probably due to the large uncertainties of the measurements. At $z \sim 12$, we also fit only the measurements of this study, excluding the brightest data point in Harikane et al. (2022a), as shown in Figure 14. The best-fit DPL and Schechter functions are slightly flatter than the fitting results with the data point in Harikane et al. (2022a) at the bright end.

Figure 15 presents the redshift evolution of the luminosity function. We find the continuous decrease in the luminosity functions from $z \sim 5$ to $z \sim 12$. We do not find a significant decrease from $z \sim 12$ to 16 beyond the uncertainty. There is a hint of a small evolution from $z \sim 12$ to 16, while the small number statistics does not allow us to conclude whether the evolutionary trend changes from $z \sim 5-12$ to 12-16.

Figure 16 compares the observed luminosity functions at $z \sim 12$ and 16 with those predicted by theoretical models (Dayal et al. 2014, 2019; Behroozi et al. 2020; Yung et al. 2020; Mason et al. 2023; Wilkins et al. 2023). At $z \sim 12$, most of the models in Figure 16 explain the observational measurements in the faint magnitude range from -20 to -18 mag, while some models do not reproduce the moderately high number densities of the observational measurements at the bright magnitude of $M_{\text{UV}} < -20$ mag. At $z \sim 16$, most of the models cannot reproduce the observed number density of bright galaxies at $M_{\text{UV}} < -20$ mag, except for the FLARES (Lovell et al. 2021; Vijayan et al. 2021; Wilkins et al. 2023) whose prediction at $z \sim 15$ agrees with our number density estimate within uncertainties. Similarly, Figure 17 shows the predicted number of bright galaxies at $z \sim 12-16$ with $M_{\text{UV}} < -20$ mag. Figure 17 indicates that the models under-predict the number of galaxies compared to the observation, although the significance is small, and more data are needed to obtain the conclusion. This difference of the observations and models would suggest that the feedback effects in the models may be too strong to produce abundant bright galaxies, lower dust obscuration in these bright galaxies than the model

assumptions, and/or that there exist hidden AGNs that produce radiation comparable with or more than stellar components of the galaxies (e.g., Bowler et al. 2014, 2020; Ono et al. 2018; Stevans et al. 2018; Harikane et al. 2022b; Mason et al. 2023; Pacucci et al. 2022; Shibuya et al. 2022), although there is also a possibility that this difference may be caused by other physical processes, as discussed in Section 6.

5.3. Cosmic Star Formation Rate Density

We derive the cosmic SFR densities at $z \sim 9, 12$, and 16. We integrate the best-fit double-power-law functions (Table 8) down to -17 mag, the same limit as previous studies (e.g., Bouwens et al. 2015; Oesch et al. 2018; Harikane et al. 2022a), and obtain the UV luminosity densities, ρ_{UV} . We correct ρ_{UV} for the dust extinction, following the attenuation-UV slope (β_{UV}) relation (Meurer et al. 1999) and $\beta_{\text{UV}}-M_{\text{UV}}$ relation at $z = 8$ in Bouwens et al. (2014). The choice of these assumptions (e.g., using the attenuation-UV slope law in de Barros et al. 2014 instead) does not affect our conclusions because the correction factor is very small ($\lesssim 0.1$ dex). We calculate SFRs from UV luminosities, L_{UV} , corrected for dust extinction by the relation,

$$\text{SFR}(M_{\odot} \text{ yr}^{-1}) = \mathcal{K}_{\text{UV}} L_{\text{UV}} (\text{erg s}^{-1} \text{ Hz}^{-1}), \quad (12)$$

where \mathcal{K}_{UV} is the conversion factor that depends on the recent star formation history, metal enrichment history, and choice of the IMF. Here we apply $\mathcal{K}_{\text{UV}} = 1.15 \times 10^{-28} M_{\odot} \text{ yr}^{-1} / (\text{erg s}^{-1} \text{ Hz}^{-1})$, which is used in Madau & Dickinson (2014). This value of \mathcal{K}_{UV} is valid for the Salpeter (1955) IMF, and consistent with the cosmic star formation history and the evolved stellar metallicity ($10^{-0.15z} Z_{\odot}$; Madau & Dickinson 2014) up to $z \sim 10$. Table 9 summarizes our measurements of the cosmic UV luminosity density and SFR densities without and with dust extinction correction at each redshift.

Figure 18 presents the cosmic SFR density evolution. In this figure, we show the cosmic SFR density measurements at $z \sim 0-10$ obtained by previous studies, all of which are converted to the calibration of Madau & Dickinson (2014) with the Salpeter (1955) IMF (Equation (12)). We confirm that

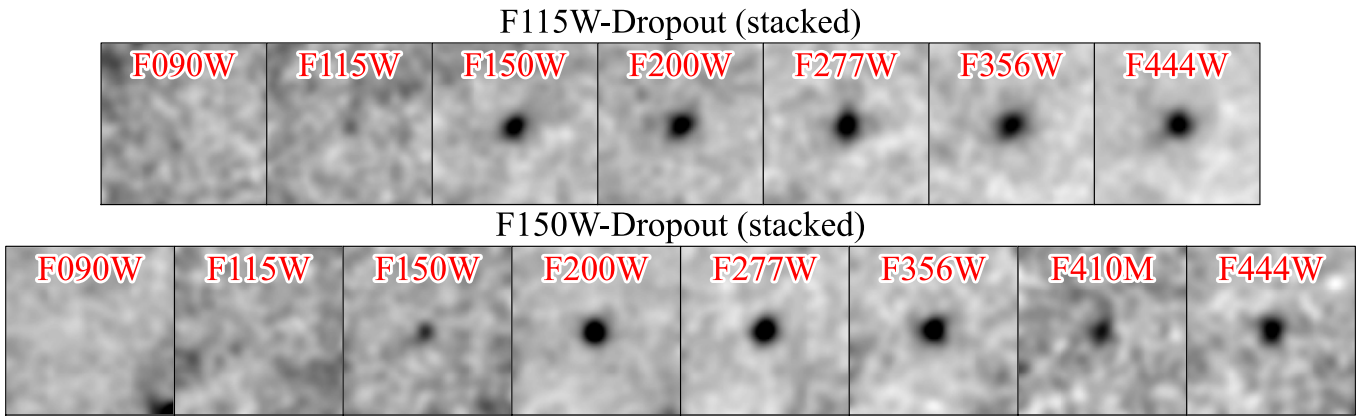


Figure 11. Stacked images of our F115W dropouts (top) and F150W dropouts (bottom). The size of the images is $1''.5 \times 1''.5$. There are no positive signals found at the positions of the dropouts in the F090W image (top) and the F090W and F115W images (bottom) whose wavelength ranges (rest frame $< 1216 \text{ \AA}$) do not include emission from $z \sim 9$ and 12 sources, indicating that our samples are not significantly contaminated by foreground interlopers.

Table 6

Summary of Magnification Factors Estimated by Various Mass Models

ID (1)	z (2)	μ_{glafic} (3)	μ_{M22} (4)	μ_{P22} (5)	μ_{C22} (6)
SM-z12-1	$12.47^{+1.19}_{-0.72}$	1.22	1.11	1.00	1.00
s04590	8.495	8.69	5.81	6.90	7.42
s06355	7.664	1.78	1.68	1.43	1.68
s10612	7.659	1.86	1.68	1.61	1.66

Note. (1) Name. (2) Spectroscopic or photometric redshift. (3)–(6) Magnification factors estimated by GRAFIC, Mahler et al. (2022), Pascale et al. (2022), and Caminha et al. (2022).

our SFR density at $z \sim 9$ is consistent with previous measurements. We compare the observational measurements of the SFR densities with the constant star formation efficiency (SFR/ $M_{\text{h}}(z) = \text{const.}$) model (Harikane et al. 2022b) together with the extrapolation of the Madau & Dickinson (2014) estimates at $z = 0$ –8. We find that the cosmic SFR densities significantly decrease from $z \sim 9$ to 12. A decrease in the cosmic SFR densities may exist from $z \sim 12$ to 16, while the decrease is not larger than the errors. Interestingly, the constant star formation efficiency model explains the evolution of the cosmic SFR densities up to $z \sim 10$ (Harikane et al. 2022b), while our measurement at $z \sim 12$ is higher than the model prediction beyond the uncertainty. Moreover, there is a hint of a high cosmic SFR density at $z \sim 16$ above the model, although it is not statistically significant due to the large error. Such higher SFR densities than the constant efficiency model at $z \sim 15$ are actually consistent with observations of Balmer-break galaxy candidates at $z \sim 6$ (Mawatari et al. 2020a).

6. Discussion

6.1. Possible High Cosmic Star Formation Rate Density at $z > 10$

Our observational measurements suggest that the SFR densities at $z \sim 12$ –16 are higher than the constant star formation efficiency model of Harikane et al. (2022b). Although the constant star formation efficiency model well explains the cosmic SFR densities at $z \sim 0$ –10, this model underpredicts those at $z \sim 12$ –16. Here we discuss the

following three possibilities that explain the observed high SFR densities at $z \sim 12$ –16.

- (A) *No star formation suppression at the pre-reionization epoch.* The universe at $z \sim 12$ –16 is at the pre-reionization epoch when the IGM is highly neutral (Ouchi et al. 2020; Robertson 2022). At the epoch of reionization (EoR; $z \sim 6$ –12) and the epoch of post-reionization (post-EoR; $z \lesssim 6$), galaxies and AGNs produce UV radiation by their star formation and nuclear activity, and produce strong UV background radiation. The UV background radiation heats up H I gas in low-mass halos of $M_{\text{h}} \lesssim 10^{8-9} M_{\odot}$ with negligible H I self-shielding, suppressing star formation at the EoR and post-EoR (Barkana & Loeb 2000; Susa & Umemura 2004; Hoeft et al. 2006; Mesinger et al. 2009; Pawlik & Schaye 2009; Sawala et al. 2010; Bland-Hawthorn et al. 2015). Although the halo masses of our galaxies at $z \sim 12$ –16 are unknown, the maximum halo mass existing at $z \sim 15$ given the survey volume of this study is $M_{\text{h}} \simeq 3 \times 10^9 M_{\odot}$ in the structure formation model with the Planck cosmology (Behroozi et al. 2020). In other words, most halos (with $\lesssim 10^9 M_{\odot}$) at $z \sim 15$ are not affected by the UV background at the pre-reionization epoch, while similar halos at $z \lesssim 10$ experience the suppression of star formation by the UV background at the EoR and post-EoR. To test whether this effect can quantitatively explain the observed SFR densities, we construct a model of the SFR density evolution including the enhancement of the star formation that is free from the suppression by the UV background at the pre-EoR. We use the model in Barkana & Loeb (2000) with a reionization redshift of $z_{\text{reion}} = 13$ and multiply the prediction of the constant star formation efficiency model (Harikane et al. 2022b) by a factor of the SFR enhancement due to the lack of suppression by the UV background in Barkana & Loeb (2000). The left panel of Figure 19 presents this hybrid model including the effect of star formation enhancement at the pre-EoR, which reproduces the observed SFR densities at $z \sim 12$ –16 within uncertainties. This agreement indicates a possibility that the star formation efficiency at $z \sim 12$ –16 is higher than that at $z \lesssim 10$ due

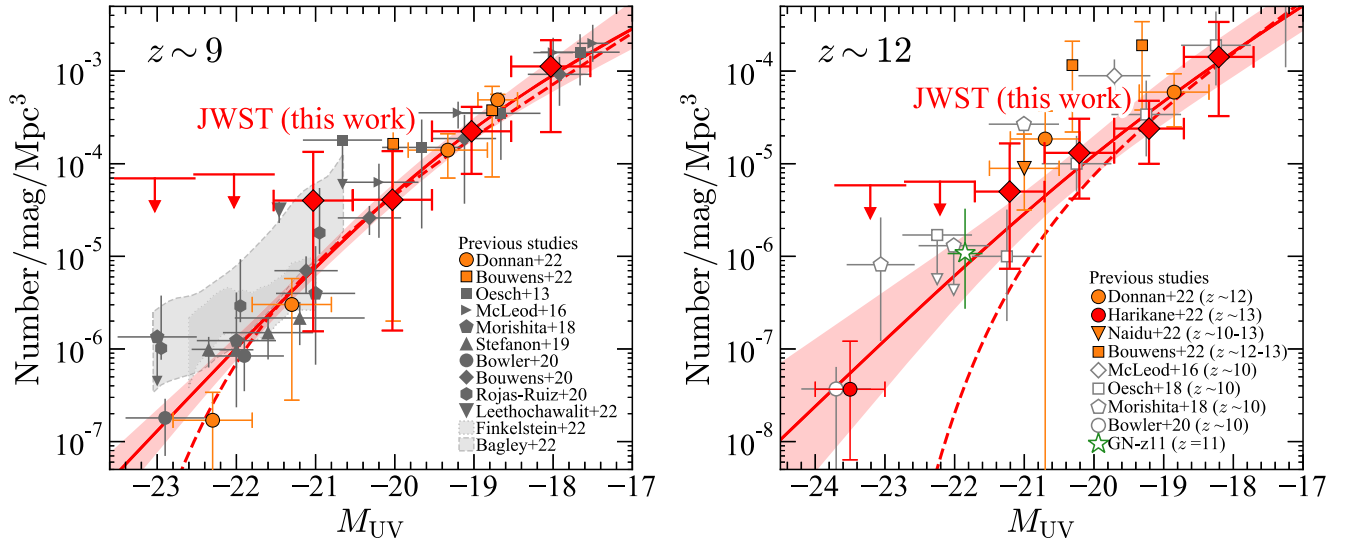


Figure 12. UV luminosity functions at $z \sim 9$ (left) and 12 (right). The red diamonds represent the number densities of our galaxy candidates, while the red arrows indicate the 1σ upper limits. The errors include cosmic variance (see text). The red solid and dashed lines are our best-fit double-power-law and Schechter functions, respectively. In the left panel, the orange circles indicate the luminosity functions at $z \sim 9$ obtained in Donnan et al. (2023) using JWST data, and the gray symbols and shades denote the results at $z \sim 9$ derived by the previous studies using HST or ground-based telescope data: Oesch et al. (2013; squares), McLeod et al. (2016; right-pointing triangles), Morishita et al. (2018; pentagons), Stefanon et al. (2019; triangles), Bowler et al. (2020; diamonds), Rojas-Ruiz et al. (2020; hexagons), Leethochawalit et al. (2022; down-pointing triangle), Finkelstein et al. (2022a; shade with dotted lines), and Bagley et al. (2022b; shade with dashed lines). In the right panel, the orange circles, the red circle, the orange down-pointing triangle, and the orange squares indicate the number density of galaxies at $z \sim 12$, $z \sim 13$, $z \sim 10-13$, and $z \sim 12-13$ reported by Donnan et al. (2023), Harikane et al. (2022a), Naidu et al. (2022b), and Bouwens et al. (2022b), respectively. The gray open symbols indicate the luminosity functions at $z \sim 10$ obtained by McLeod et al. (2016; diamonds), Oesch et al. (2018; squares), Morishita et al. (2018; pentagons), and Bowler et al. (2020; circle). The green open star mark represents the number density of GN-z11 (Oesch et al. 2016). See Harikane et al. (2022a) for an estimate of the number density and the UV magnitude of GN-z11. Our estimated luminosity functions at $z \sim 9$ and 12 agree well with previous HST and JWST results.

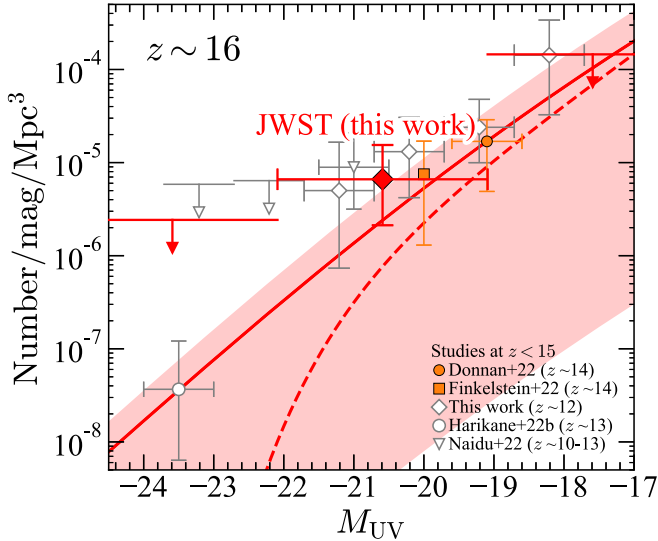


Figure 13. UV luminosity function at $z \sim 16$. The red diamond and the arrows represent the number density of our galaxy candidates and the 1σ upper limits, respectively. For reference, we show the UV luminosity functions at the lower redshifts, $z \sim 14$ (Donnan et al. 2023; orange filled circle), $z \sim 14$ (Finkelstein et al. 2022b; orange filled square), $z \sim 12$ (this study; gray open diamonds), $z \sim 13$ (Harikane et al. 2022a; gray open circle), and $z \sim 10-13$ (Naidu et al. 2022b; gray open down-pointing triangle).

to the lack of suppression of star formation activity at the pre-EoR.

(B) *Presence of AGN activity.* Another possibility is that a large fraction of the observed UV luminosity densities at $z \sim 12-16$ are produced by AGNs, and there are no excessive SFR densities at $z \sim 12-16$ beyond the constant star formation efficiency model. This is an interesting

Table 7
Obtained Luminosity Function at each Redshift

M_{UV} (ABmag)	Φ ($\text{Mpc}^{-3} \text{mag}^{-1}$)
F115W Dropouts ($z \sim 9$)	
-23.03	$< 6.95 \times 10^{-5}$
-22.03	$< 7.67 \times 10^{-5}$
-21.03	$(4.00_{-3.85}^{+9.42}) \times 10^{-5}$
-20.03	$(4.08_{-3.92}^{+9.60}) \times 10^{-5}$
-19.03	$(2.24_{-1.46}^{+1.87}) \times 10^{-4}$
-18.03	$(1.12_{-0.90}^{+1.03}) \times 10^{-3}$
F150W Dropouts ($z \sim 12$)	
-23.21	$< 5.85 \times 10^{-6}$
-22.21	$< 6.40 \times 10^{-6}$
-21.21	$(5.00_{-4.27}^{+11.56}) \times 10^{-6}$
-20.21	$(1.31_{-0.89}^{+1.75}) \times 10^{-5}$
-19.21	$(2.40_{-1.30}^{+2.38}) \times 10^{-5}$
-18.21	$(1.42_{-1.10}^{+1.97}) \times 10^{-4}$
F200W Dropouts ($z \sim 16$)	
-23.59	$< 2.42 \times 10^{-6}$
-20.59	$(6.62_{-4.49}^{+8.84}) \times 10^{-6}$

Note. Errors and upper limits are 1σ .

scenario that mitigates the existence of supermassive black holes (SMBH) at $z \sim 7$ (Mortlock et al. 2011; Bañados et al. 2018; Wang et al. 2021) by efficient gas accretion on SMBHs creating AGNs, while a standard gas accretion limited by the Eddington accretion rate does not explain the existence of the SMBHs at $z \sim 7$. However, our $z \sim 12-16$ candidates except for GL-z12-1 show extended morphologies (Section 3.5). Thus the

Table 8
Fit Parameters for the Luminosity Functions

Redshift	Fitted Function	M_{UV}^* (ABmag)	$\log \phi^*$ (Mpc^{-3})	α	β	χ^2/dof
$z \sim 9$	DPL	$-19.33^{+2.24}_{-0.96}$	$-3.50^{+1.53}_{-0.65}$	-2.10(fixed)	$-3.27^{+0.34}_{-0.37}$	2.1/9
	Schechter	$-21.24^{+0.45}_{-0.59}$	$-4.83^{+0.37}_{-0.49}$	-2.35(fixed)	...	3.4/10
$z \sim 12$	DPL	-19.60(fixed)	$-4.33^{+0.22}_{-0.22}$	-2.10(fixed)	$-2.83^{+0.50}_{-0.44}$	0.8/3
	Schechter	$-20.47^{+1.94}_{-0.15}$	$-5.06^{+1.51}_{-0.17}$	-2.35(fixed)	...	1.2/3
$z \sim 16$	DPL	-19.60(fixed)	$-4.71^{+0.33}_{-2.83}$	-2.10(fixed)	$-2.70^{+0.00}_{-0.00}$	1.4/1
	Schechter	-20.80(fixed)	$-5.84^{+0.47}_{-4.03}$	-2.35(fixed)	...	1.9/2
$z \sim 12^a$	DPL	-19.60(fixed)	$-4.32^{+0.22}_{-0.22}$	-2.10(fixed)	$-2.21^{+1.07}_{-1.06}$	0.3/2
	Schechter	$-21.97^{+2.88}_{-0.11}$	$-5.95^{+1.84}_{-0.18}$	-2.35(fixed)	...	0.5/2

Notes. Errors are 1σ .

^a Fit parameters without the brightest data point in Harikane et al. (2022a), which are shown in Figure 14.

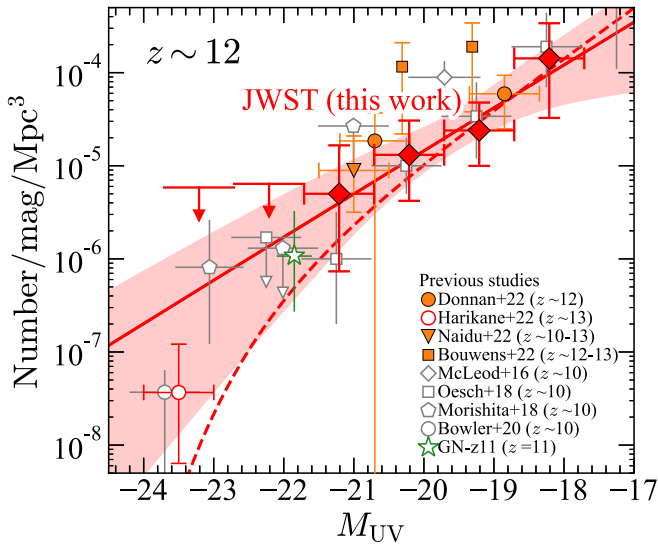


Figure 14. Same as the right panel of Figure 12, but with the fitting results without the brightest data point in Harikane et al. (2022a).

fraction of AGN-radiation-dominated galaxies is as small as $\sim 10\%$ ($=1/10$) at $z \sim 12-16$. Although the excessive SFR density estimate at $z \sim 16$ is unclear due to the small statistics, the one at $z \sim 12$ cannot be explained by AGN activity.

- (C) *A top-heavy IMF.* The third possibility is an overestimate of the SFR density due to a top-heavy IMF possibly with a Population III stellar population. In our estimate of the SFR density, we use the canonical UV luminosity-to-SFR conversion factor of $\mathcal{K}_{UV} = 1.15 \times 10^{-28} M_{\odot} \text{ yr}^{-1} / (\text{erg s}^{-1} \text{ Hz}^{-1})$, which is for the Salpeter (1955) IMF, while \mathcal{K}_{UV} depends on star formation history, metallicities, and IMFs (e.g., Madau & Dickinson 2014; Tacchella et al. 2018). Indeed in the early universe, the IMF is expected to be more top-heavy because of a lower metallicity or a higher CMB temperature (e.g., Omukai et al. 2005; Chon et al. 2022), resulting in a higher Jeans mass, especially for Population III stellar populations (e.g., Hirano et al. 2014, 2015). To test whether this effect can explain the observed densities, we calculate the UV-to-SFR conversion factor, \mathcal{K}_{UV} , for different metallicity and IMF assumptions using YGGDRASIL (Zackrisson et al. 2011). Figure 20

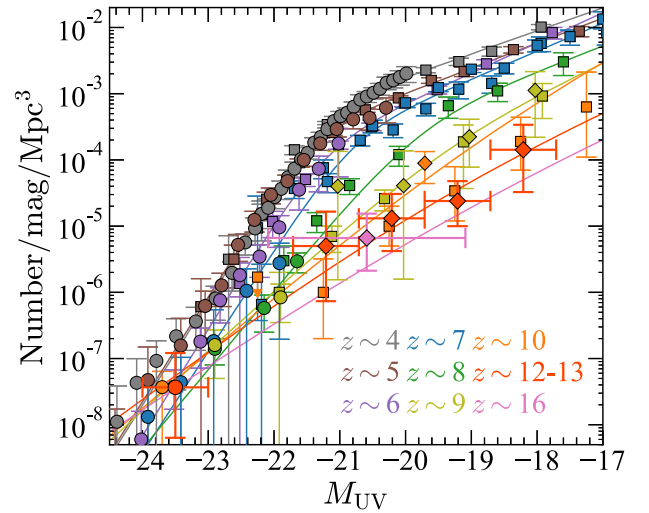


Figure 15. Evolution of the UV luminosity functions from $z \sim 4$ to $z \sim 16$. The yellow, red, and pink diamonds represent our measurements of the luminosity functions at $z \sim 9, 12,$ and $16,$ respectively, whereas the red circle is the one obtained by Harikane et al. (2022a) at $z \sim 13$. The orange, yellow, green, blue, purple, brown, and gray symbols indicate the luminosity functions at $z \sim 10, 9, 8, 7, 6, 5,$ and $4,$ respectively. The circles at $z \sim 4-7$ and $8-10$ are the data taken from Harikane et al. (2022b) and Bowler et al. (2020), respectively. The squares at $z \sim 4-9$ and $z \sim 10$ are the data of Bouwens et al. (2021) and Oesch et al. (2018), respectively. The diamond at $z \sim 10$ represents the result of McLeod et al. (2016). The lines denote the double-power-law functions derived by the previous studies for $z \sim 4-7$ (Harikane et al. 2022b) and $z \sim 8-13$ (Bowler et al. 2020). For clarity, we shift the data point of Bowler et al. (2020) at $z \sim 10$ by -0.2 mag.

presents \mathcal{K}_{UV} for different metallicities and IMFs as a function of the stellar age. We find that Population III stellar populations with top-heavy IMFs (PopIII.1 and PopIII.2 in YGGDRASIL) produce $\sim 3-4$ times more UV photons than the canonical assumption given the SFR, because nebular continuum emission boosts the UV luminosity as discussed in previous studies (e.g., Zackrisson et al. 2008; Schaerer & de Barros 2009, 2010). This low conversion factor reduces the SFR density estimates at $z \sim 12-16$ as shown in the right panel of Figure 19, resulting in SFR densities consistent with the constant star formation efficiency model.

Based on these discussions, we conclude that (A) *a lack of star formation suppression at the pre-reionization epoch* or

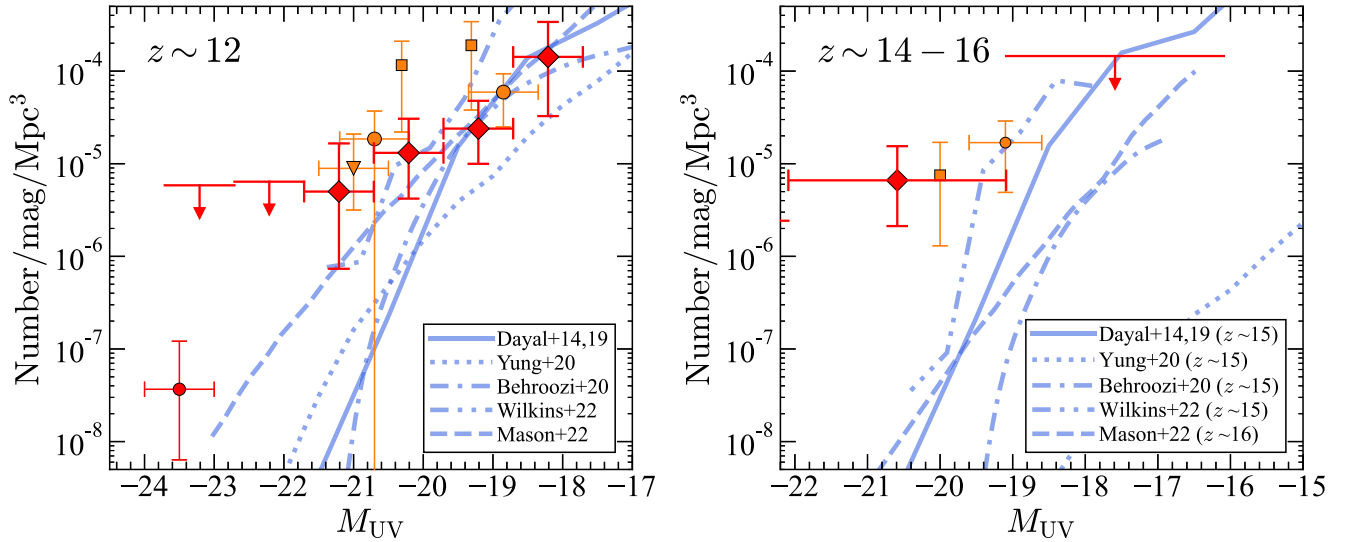


Figure 16. Comparison of the luminosity function measurements with theoretical predictions and the empirical models at $z \sim 12$ (left) and $z \sim 16$ (right). The blue lines show the theoretical and empirical models obtained by Dayal et al. (2014, 2019; solid line), Yung et al. (2020; dotted line), Behroozi et al. (2020; dotted–dashed line), Wilkins et al. (2023; double-dotted–dashed line), and Mason et al. (2023, their no dust model; dashed line). The red and orange symbols show observational results in the same manner as Figures 12 and 13. The red diamonds and arrows represent the measurements and upper limits obtained by this study. The orange circles, the red circle, the down-pointing orange triangle, and the orange square in the left (right) panel indicate the number densities reported by Donnan et al. (2023), Harikane et al. (2022a), Naidu et al. (2022b), and Bouwens et al. (2022b) and Finkelstein et al. (2022b), respectively.

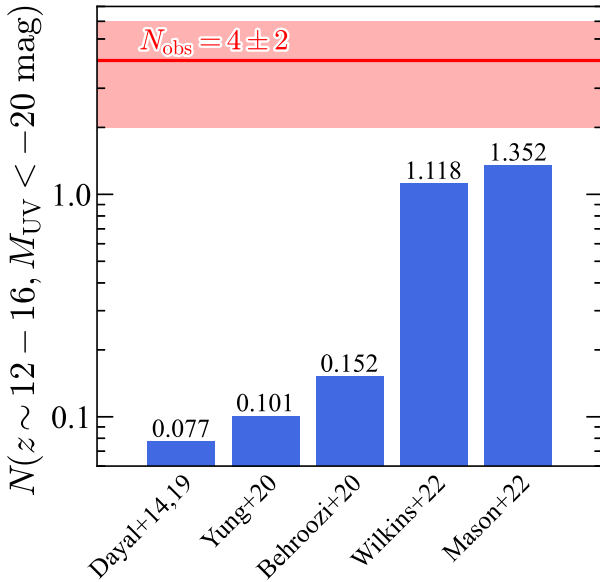


Figure 17. Theoretical predictions for the number of bright galaxies at $z \sim 12-16$ with $M_{UV} < -20$ mag detected in our survey area of ~ 90 arcmin². These numbers are based on the theoretical models of Dayal et al. (2014, 2019), Yung et al. (2020), Behroozi et al. (2020), Wilkins et al. (2023), and Mason et al. (2023). The red horizontal line with the shaded region indicates the number of observed galaxies at $z \sim 12-16$ with $M_{UV} < -20$ mag ($N_{\text{obs}} = 4 \pm 2$), which is higher than these model predictions.

Table 9
Obtained Cosmic UV Luminosity Density and SFR Density

Redshift	$\log \rho_{UV}$ ($\text{erg s}^{-1} \text{Hz}^{-1} \text{Mpc}^{-3}$)	$\log \rho_{SFR,UV}$ ($M_{\odot} \text{yr}^{-1} \text{Mpc}^{-3}$)	$\log \rho_{SFR}$ ($M_{\odot} \text{yr}^{-1} \text{Mpc}^{-3}$)
$z \sim 9$	$25.28^{+0.19}_{-0.16}$	$-2.65^{+0.19}_{-0.16}$	$-2.61^{+0.18}_{-0.16}$
$z \sim 12$	$24.61^{+0.26}_{-0.26}$	$-3.33^{+0.26}_{-0.26}$	$-3.23^{+0.29}_{-0.27}$
$z \sim 16$	$24.24^{+0.33}_{-2.83}$	$-3.70^{+0.33}_{-2.83}$	$-3.59^{+0.33}_{-2.83}$

Note. Errors are 1σ . $\rho_{SFR,UV}$ and ρ_{SFR} are the SFR densities without and with dust extinction correction, respectively.

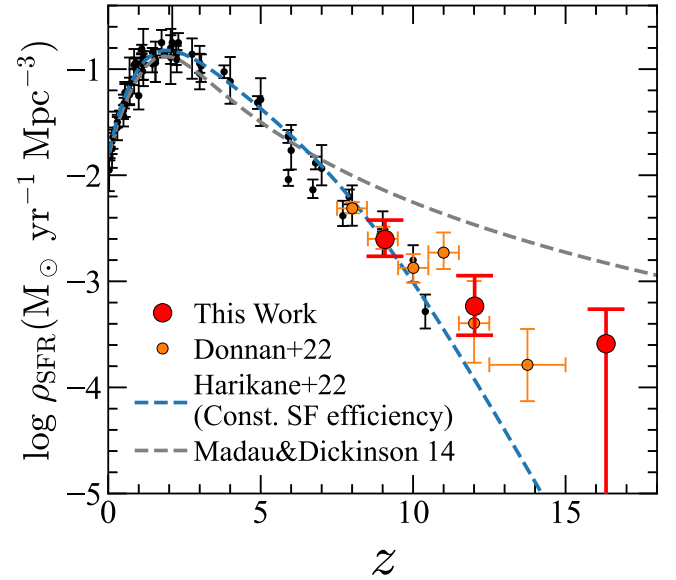


Figure 18. Cosmic SFR density evolution. The red circles represent the cosmic SFR densities obtained by our study, with the double-power-law luminosity functions integrated down to $M_{UV} = -17$ mag. The black circles indicate the cosmic SFR densities derived by Madau & Dickinson (2014), Finkelstein et al. (2015a), McLeod et al. (2016), Bhatwadekar et al. (2019), and Bouwens et al. (2020). The orange circles are results by Donnan et al. (2023). The blue dashed curve is the best-fit function of the cosmic SFR densities in Harikane et al. (2022b, their Equation (60)). In Harikane et al. (2022b), they assume a constant star formation efficiency at $z > 10$, resulting in the power-law decline with $\rho_{SFR} \propto 10^{-0.5(1+z)}$. The gray dashed curve shows the best-fit function at $z \lesssim 8$ determined by Madau & Dickinson (2014) extrapolated to $z > 8$. All results are converted to those of the Salpeter (1955) IMF.

(C) a top-heavy IMF with a Population III–like star formation can explain the observed high SFR densities at $z \sim 12-16$. These possibilities can be further investigated by follow-up observations with JWST/MIRI covering a longer wavelength than the Balmer break to obtain the robust stellar mass measurements and star formation history, or with JWST/NIRSpec and MIRI spectroscopy to search for

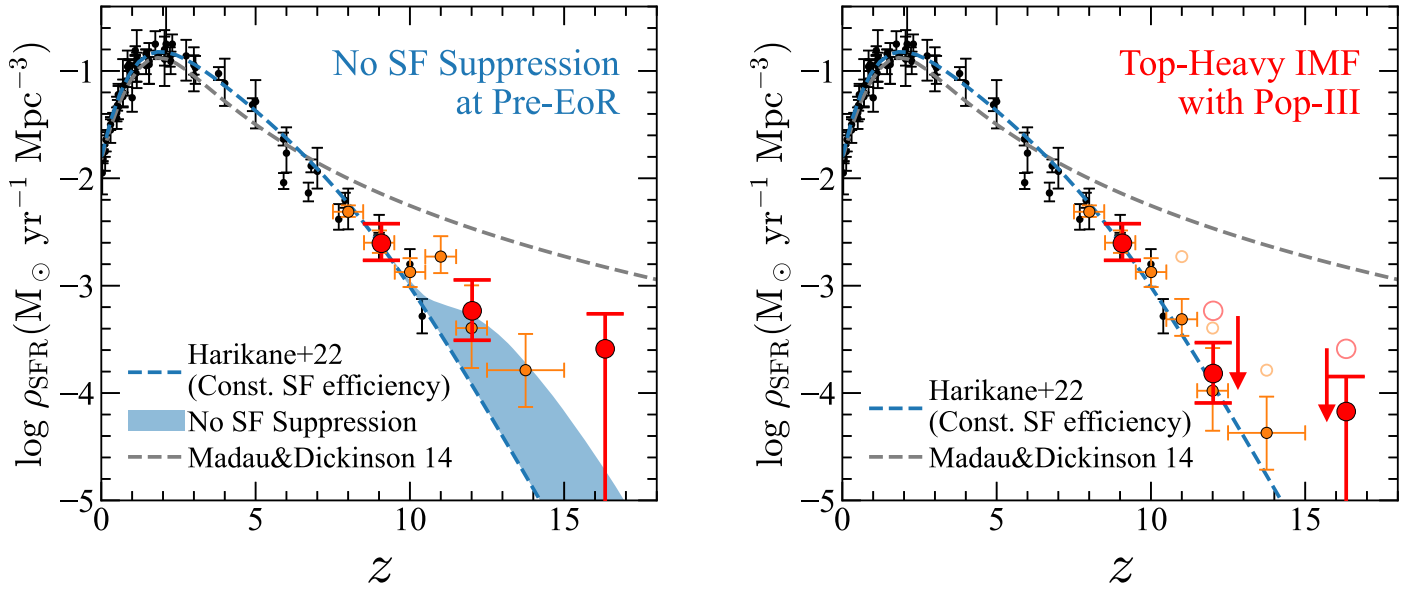


Figure 19. Possible scenarios to explain the observed SFR densities at $z > 10$. (Left) Scenario of no star formation suppression at the pre-reionization epoch. At the reionization epoch and after that, star formation in low-mass halos is suppressed by strong UV background radiation, while before the reionization epoch such a suppression of star formation activity does not occur. The upper edge of the blue shaded region indicates the enhancement of the star formation by this effect (Barkana & Loeb 2000), which explains the observed SFR densities (see texts for details). (Right) Scenario of Population III star formation. As shown in Figure 20, Population III stellar populations with a top-heavy IMF produces a significant amount of UV photons at a given SFR, resulting in the overestimates of the SFR densities if we use the canonical UV–SFR conversion factor. The red and orange filled circles at $z > 10.5$ are SFR densities calculated based on the conversion factor for a Population III stellar population with a top-heavy IMF (the PopIII.1 model in Figure 20), which agree well with the constant star formation efficiency model in Harikane et al. (2022b). The open circles are the SFR densities based on the canonical conversion factor.

signatures of Population III–like stellar populations and AGN activity.

6.2. Properties of Luminous Galaxy Candidates

In this study, we have found several luminous galaxy candidates at the early epoch of $z \sim 10$ –16, when the age of the universe is only ~ 200 –500 Myr after the Big Bang. Here we discuss the physical properties of these luminous galaxy candidates.

Table 10 summarizes the SFRs and stellar masses of six galaxy candidates whose UV magnitudes are brighter than $M_{UV} = -19.5$ mag, constrained by the SED fitting in Section 3.3 assuming the Chabrier (2003) IMF. Our estimates of the SFRs and stellar masses agree with previous estimates by Naidu et al. (2022b), Donnan et al. (2023), and Finkelstein et al. (2022b), indicating that these luminous galaxies are very massive with stellar masses as high as $M_* \sim (1-10) \times 10^8 M_\odot$ at $z \sim 10$ –16. While the contributions from AGN radiation to the SEDs may be suspected in one of the objects, GL-z12-1 (see Sections 3.5 and 6.1), at least the rest of the objects (i.e., $\sim 80\%$ of the bright $z \sim 10$ –16 galaxies) would be truly stellar massive. Although the NIRCcam photometry is limited to $< 5 \mu\text{m}$ and does not trace the SEDs beyond the Balmer break (4000 \AA) corresponding to 5 – $7 \mu\text{m}$ in the observed frame at $z \sim 10$ –16, these stellar mass estimates provide rough lower limits that miss the contribution from old stellar populations beyond the Balmer break, given high specific SFRs of these galaxy candidates, $\text{SFR}/M_* \sim 10^{-8} \text{ yr}^{-1}$.

There is the question of how these galaxies with large stellar masses form at this early epoch of $z \sim 10$ –16. To discuss the formation scenario of these massive galaxy candidates, we estimate the stellar-to-halo mass ratio (SHMR) of these galaxies. Using the abundance-matching technique in the same manner as Harikane et al. (2016, their Equation (66)), we

estimate the halo mass of the most massive halo that can be observed with the survey volume in this study, resulting in $5 \times 10^{10} M_\odot$ and $5 \times 10^9 M_\odot$ at $z \sim 12$ and $z \sim 16$, respectively. From the stellar mass estimates discussed above, the SHMRs of $z \sim 12$ and $z \sim 16$ galaxies are ~ 0.01 and ~ 0.1 , respectively. Because the cosmic baryon to dark matter density ratio is $\Omega_b/\Omega_m = 0.16$ (Planck Collaboration et al. 2020), the SHMRs of the $z \sim 16$ galaxies reach $\sim 60\%$ of the cosmic baryon fraction, as shown in Figure 21. In other words, more than a half of the baryon gas in the halos is converted to stars, which is unlikely found in lower-redshift and present-day galaxies whose SHMRs are ~ 0.02 – 0.03 at maximum (e.g., Harikane et al. 2016; Behroozi et al. 2019). A similar conclusion is obtained from the comparison of the UV luminosity functions (Inayoshi et al. 2022). However, theoretical models predict such efficient star formation at the pre-reionization epoch where 70% – 80% of baryon are converted stars (Susa & Umemura 2004) in halos with 10^8 – $10^9 M_\odot$ masses in a few hundred Myr, when the UV background radiation is too weak to suppress star formation (see discussion (A) in Section 6.1). The other four galaxies at $z \sim 11$ –14 also show higher stellar masses compared to the predictions from the maximum SHMR in Behroozi et al. (2020), indicating elevated star formation efficiencies, probably due to the lack of suppression of star formation activity at the pre-reionization epoch. Another possibility is that the SFRs and the stellar masses of these bright galaxies are overestimated due to the assumption of the IMF and metallicity in the SED fitting, as discussed in Section 6.1 (discussion (C)). Indeed, if we assume that the stellar population of these galaxies is dominated by Population III with a top-heavy IMF, the SFR and stellar mass are reduced by a factor of ~ 3 – 4 , more comparable to the observed SHMRs at lower redshifts. These comparisons, together with the discussions in Section 6.1, indicate that the

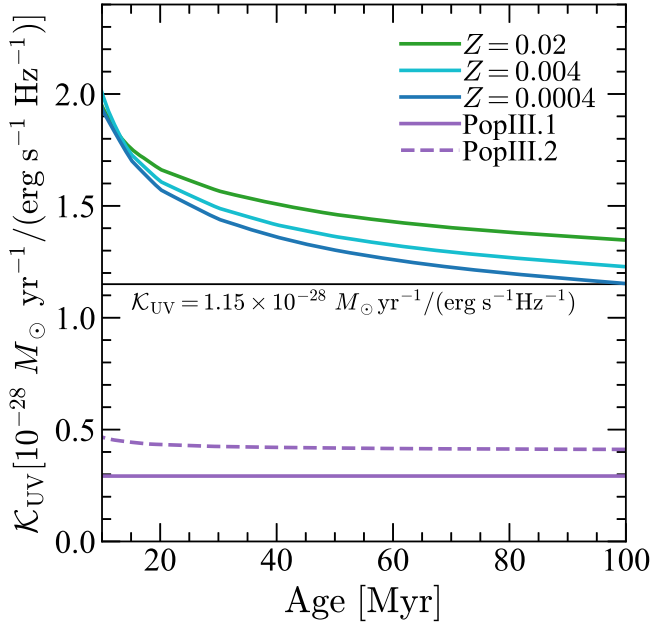


Figure 20. UV luminosity-SFR conversion factor, \mathcal{K}_{UV} , for various metallicities as a function of the stellar age. The green, cyan, and blue curves show the conversion factor for metallicities of $Z = 0.02$, 0.004 , 0.0004 , respectively, calculated with YGGDRASIL (Zackrisson et al. 2011) assuming a constant star formation history with a unity gas covering fraction. These factors are values for a UV luminosity at 1500 \AA in the Salpeter (1955) IMF in the interval of $0.1\text{--}100 M_{\odot}$. Note that the original outputs from YGGDRASIL are for the Kroupa (2001) IMF, and we correct for the IMF difference by multiplying the outputs by 1.49. The solid (PopIII.1) and dashed (PopIII.2) purple curves show the conversion factors for Population III stellar populations with an extremely top-heavy IMF ($50\text{--}500 M_{\odot}$, the Salpeter 1955 slope) and a moderately top-heavy IMF (log-normal with characteristic mass of $M_c = 10 M_{\odot}$, dispersion $\sigma = 1 M_{\odot}$, and wings extending from 1 to $500 M_{\odot}$). If galaxies at $z > 10$ are dominated by Population III stellar populations, the conversion factor is significantly lower than the typically assumed value ($\mathcal{K}_{\text{UV}} = 1.15 \times 10^{-28} M_{\odot} \text{ yr}^{-1} / (\text{erg s}^{-1} \text{ Hz}^{-1})$; black line), resulting in the overestimation of the SFR.

Table 10

SFRs and Stellar Masses of Luminous Galaxy Candidates with $M_{\text{UV}} < -19.5$ mag

ID	z_{phot}	SFR ($M_{\odot} \text{ yr}^{-1}$)	M_* (M_{\odot})
GL-z9-1	$10.49^{+0.53}_{-0.72}$	$14.2^{+25.0}_{-11.2}$	$(1.1^{+3.4}_{-0.9}) \times 10^9$
CR2-z12-1	$11.63^{+0.51}_{-0.53}$	$0.9^{+4.9}_{-0.1}$	$(7.6^{+60.4}_{-3.5}) \times 10^7$
GL-z12-1 ^a	$12.28^{+0.08}_{-0.07}$	$2.9^{+10.9}_{-1.0}$	$(2.3^{+16.0}_{-1.1}) \times 10^8$
S5-z12-1	$12.58^{+1.23}_{-0.46}$	$5.5^{+4.7}_{-4.4}$	$(3.4^{+10.3}_{-2.7}) \times 10^8$
CR2-z16-1	$16.25^{+0.24}_{-0.46}$	$31.2^{+25.8}_{-30.8}$	$(1.6^{+16.8}_{-1.3}) \times 10^9$
S5-z16-1	$16.41^{+0.66}_{-0.55}$	$5.1^{+21.7}_{-1.8}$	$(3.9^{+62.4}_{-2.0}) \times 10^8$

Notes. Assuming the Chabrier (2003) IMF and metallicity of $Z = 0.2 Z_{\odot}$. The SFR is averaged over the past 50 Myr in the same manner as Tacchella et al. (2022). See Section 3.3 for the details of the SED fitting.

^a This candidate shows a compact morphology indicative of AGN activity, while the profile is spatially extended more than the PSF (Section 3.5).

observed properties of $z \sim 10\text{--}16$ galaxies (i.e., high cosmic SFR densities and massive stellar masses) can be explained by either the lack of star formation suppression by UV background radiation at the pre-reionization epoch or a top-heavy IMF possibly with a Population III-like stellar population.

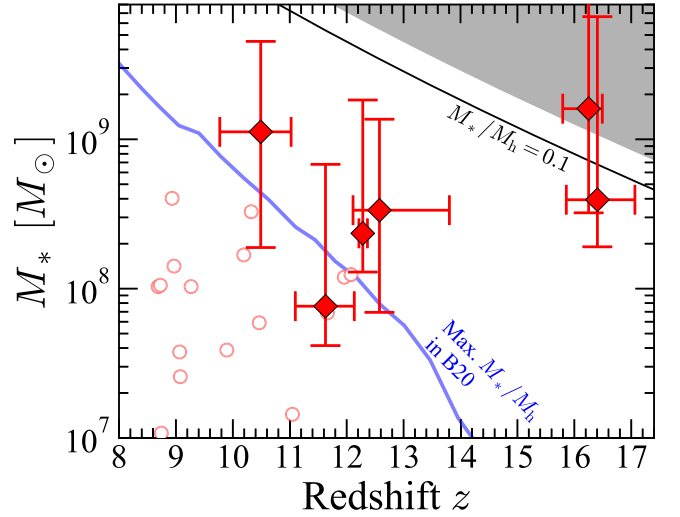


Figure 21 Stellar masses of our galaxy candidates as a function of the redshift. The red filled diamonds show the stellar mass estimates for six luminous galaxy candidates with $M_{\text{UV}} < -19.5$ mag at $z \sim 10\text{--}16$ (Table 10), and the open red circles are the results for other candidates. The gray shaded region indicates the stellar mass whose number density is below the observational limit, calculated from the cosmic baryon fraction ($\Omega_b/\Omega_m = 0.16$) and the maximum halo mass that can be observed with the survey volume of this study. The black and blue curves indicate the stellar masses calculated from the maximum halo mass with $M_*/M_h = 0.1$ and the maximum M_*/M_h value at each redshift in Behroozi et al. (2020), respectively. The massive stellar masses ($M_* \sim 10^9 M_{\odot}$) of the two $z \sim 16$ candidates can be explained by a very high SHMR of $M_*/M_h = 0.1$, indicating a star formation efficiency as high as $\sim 60\%$. The other four luminous candidates at $z \sim 10\text{--}13$ also show higher stellar masses compared to the predictions from Behroozi et al. (2020).

7. Summary

In this paper, we have conducted comprehensive analyses for the JWST/NIRCam images taken by the JWST ERO SMACS J0723, Stephan’s Quintet, ERS GLASS, and CEERS projects, covering a total of $\sim 88.7 \text{ arcmin}^2$, in conjunction with the supports of the ERO SMACS J0723 NIRSpec spectra. We reduced the NIRCam data sets using the new calibration parameters released in October, based on calibration observations of three different standard stars placed in all of the 10 NIRCam detectors. Our major findings are summarized below:

1. We have selected dropout galaxy candidates at $z \sim 9$, $z \sim 12$, and $z \sim 16$ showing significant continuum breaks in the NIRCam F115W, F150W, and F200W bands, respectively, by the color criteria, confirming clear nondetections in the band(s) whose wavelength is shorter than the continuum breaks including the F090W band (Section 3.2, Figure 2). Because we have found that a weak photo- z criterion of $\Delta\chi^2 > 4$ cannot remove a number of foreground interlopers on the bases of the JWST simulation data produced by the CEERS project team (Figure 3), we apply a stringent photo- z determination criterion of $\Delta\chi^2 > 9$ with the PROSPECTOR code for our galaxy selection. We thus identify 13, 8, and 2 dropout galaxy candidates at $z \sim 9$, $z \sim 12$, and $z \sim 16$, respectively (Table 2). We confirm that our photometric redshifts agree well with the spectroscopic redshifts, by applying our photometric redshift technique to galaxies at

- $z_{\text{spec}} \sim 8\text{--}9$ found by the ERO NIRSPEC observations (Figures 4 and 5).
- We have thoroughly compared our dropout galaxy candidates with other high-redshift galaxies reported in a number of recent studies in the ERO SMACS J0723 and the ERS GLASS+CEERS NIRCcam fields. We have summarized the candidates so far claimed in the literature together with our dropouts in Tables 3–5. For bright galaxy candidates, we find that a reasonable fraction of galaxies are commonly selected in our and previous studies. We confirm that, among all of the candidates, our dropout galaxies show significant Ly α continuum breaks and flat UV continua with nondetections of continua whose wavelengths are shorter than the break (Figures 7–8), and conclude that we do not miss many reliable candidates in the redshift range of $z \sim 9\text{--}16$ in our selection.
 - We have derived the UV luminosity functions at $z \sim 9, 12,$ and 16 (Figures 12 and 13). The UV luminosity functions at $z \sim 9$ and 12 agree with those of previous HST and JWST studies within uncertainties including the cosmic variance, and the UV luminosity function at $z \sim 16$ is newly constrained. The double-power-law function is preferred to the Schechter function at $z \sim 9$, albeit with a moderately small difference of χ^2 .
 - The cosmic SFR densities at $z \sim 9, 12,$ and 16 are derived by the integration of the best-fit UV luminosity functions (Figure 18). By comparison with the previous low-redshift determinations of cosmic SFR densities, we find that the cosmic SFR densities significantly decrease from $z \sim 9$ to 12 . A decrease in the cosmic SFR densities may exist from $z \sim 12$ to 16 , while the decrease is not larger than the errors. Our measurements of the cosmic SFR density at $z \sim 12$ are higher than predictions from the constant star formation efficiency model (Harikane et al. 2022b), while the model explains the cosmic star formation history at $z \lesssim 10$. Moreover, there is a hint of a high cosmic SFR density at $z \sim 16$ above the model, although it is not statistically significant due to the large error.
 - There are several luminous and massive galaxy candidates with $M_{\text{UV}} < -19.5$ mag at the early epoch of $z \sim 10\text{--}16$, when the age of the universe is only $\sim 200\text{--}500$ Myr after the Big Bang (Figure 21). We confirm that our stellar mass estimates are comparable with those of the previous studies. Although one of the objects may have contributions of UV radiation from an AGN suggested by their morphologies, a majority ($\sim 80\%$) of the galaxies may be truly stellar massive. By comparison with the structure formation models that provide the upper limits of the dark matter halo masses observed in this study, the SHMR of the luminous galaxy candidates at $z \sim 16$ is $M_*/M_h \sim 0.1$, corresponding to $\sim 60\%$ of the baryon to dark matter density ratio in the Planck cosmology, indicating that most of baryon may be converted to stars, unlike lower-redshift and present-day galaxies with a reasonably small SHMR up to $M_*/M_h \simeq 0.02\text{--}0.03$ (e.g., Harikane et al. 2016; Behroozi et al. 2019). The other candidates at $z \sim 10\text{--}13$ also have stellar masses more massive than predictions from the maximum SHMR in Behroozi et al. (2020).

- This study identifies two interesting observational properties of galaxies at $z \sim 10\text{--}16$, the cosmic SFR densities higher than the constant star formation efficiency model and the existence of UV-luminous galaxies with high stellar masses. The possibility of the AGN contribution can be ruled out, because a small fraction of galaxies have compact morphologies suggesting no dominant radiation from the AGN activity. Instead, there are two scenarios that explain the observational properties (Figure 19). One scenario is that the UV background radiation does not suppress the star formation at the pre-reionization epoch unlike at the EoR and post-EoR. Efficient star formation may take place at $z \sim 10\text{--}16$, producing high cosmic SFR densities and stellar-massive galaxies. The other scenario is that a top-heavy IMF possibly with Population III (or similarly metal-poor) stellar populations produces strong UV radiation. The strong UV radiation may result in the overestimation of SFR densities above the constant star formation efficiency model and of the stellar mass of the luminous galaxies. Further observational and theoretical studies are needed to test these two scenarios.

We thank the anonymous referee for a careful reading and valuable comments that improved the clarity of the paper. We thank the CEERS team, especially Micaela Bagley and Steven Finkelstein, for providing many useful scripts for the NIRCcam data reduction and data sets of the CEERS-simulated images, and L. Y. Aaron Yung for providing SEDs of the mock galaxies. We are grateful to Rychard Bouwens, Seiji Fujimoto, Kohei Inayoshi, Akio Inoue, Tadayuki Kodama, Sandro Tacchella, Ken-ichi Tadaki, and Masayuki Umemura for useful comments and discussions. We thank Pratika Dayal and L. Y. Aaron Yung for sharing their data of the luminosity function. This work is based on observations made with the NASA/ESA/CSA James Webb Space Telescope. The data were obtained from the Mikulski Archive for Space Telescopes at the Space Telescope Science Institute, which is operated by the Association of Universities for Research in Astronomy, Inc., under NASA contract NAS 5-03127 for JWST. These observations are associated with programs 2732, 2736, 1324, and 1345. The authors acknowledge the ERO, GLASS, and CEERS teams led by Klaus M. Pontoppidan, Tommaso Treu, and Steven L. Finkelstein, respectively, for developing their observing programs with a zero-exclusive-access period. This publication is based upon work supported by the World Premier International Research Center Initiative (WPI Initiative), MEXT, Japan, and KAKENHI (20H00180, 20H00181, 20H05856, 21K13953, 21H04467, 22H01260) through the Japan Society for the Promotion of Science. This work was supported by the joint research program of the Institute for Cosmic Ray Research (ICRR), University of Tokyo.

Software: PANHIT (Mawatari et al. 2020b), Prospector (Johnson et al. 2021), SExtractor (Bertin & Arnouts 1996), SWarp (Bertin et al. 2002), Yggdrasil (Zackrisson et al. 2011).

ORCID iDs

Yuichi Harikane  <https://orcid.org/0000-0002-6047-430X>
 Masami Ouchi  <https://orcid.org/0000-0002-1049-6658>
 Masamune Oguri  <https://orcid.org/0000-0003-3484-399X>
 Yoshiaki Ono  <https://orcid.org/0000-0001-9011-7605>
 Kimihiko Nakajima  <https://orcid.org/0000-0003-2965-5070>
 Yuki Isobe  <https://orcid.org/0000-0001-7730-8634>

Ken Mawatari  <https://orcid.org/0000-0003-4985-0201>
 Yechi Zhang  <https://orcid.org/0000-0003-3817-8739>

References

- Adams, N. J., Conselice, C. J., Ferreira, L., et al. 2023, *MNRAS*, **518**, 4755
- Aihara, H., Aisayad, Y., Ando, M., et al. 2022, *PASJ*, **74**, 247
- Atek, H., Richard, J., Jauzac, M., et al. 2015, *ApJ*, **814**, 69
- Atek, H., Richard, J., Kneib, J.-P., & Schaerer, D. 2018, *MNRAS*, **479**, 5184
- Atek, H., Shuntov, M., Furtak, L. J., et al. 2023, *MNRAS*, **519**, 1201
- Bagley, M. B., Finkelstein, S. L., Koekemoer, A. M., et al. 2022a, arXiv:2211.02495
- Bagley, M. B., Finkelstein, S. L., Rojas-Ruiz, S., et al. 2022b, arXiv:2205.12980
- Bañados, E., Venemans, B. P., Mazzucchelli, C., et al. 2018, *Natur*, **553**, 473
- Barkana, E., & Loeb, A. 2000, *ApJ*, **539**, 20
- Barrufet, L., Oesch, P. A., Weibel, A., et al. 2022, arXiv:2207.14733
- Beckwith, S. V. W., Stiavelli, M., Koekemoer, A. M., et al. 2006, *AJ*, **132**, 1729
- Behroozi, P., Conroy, C., Wechsler, R. H., et al. 2020, *MNRAS*, **499**, 5702
- Behroozi, P., Wechsler, R. H., Hearin, A. P., & Conroy, C. 2019, *MNRAS*, **488**, 3143
- Behroozi, P. S., Wechsler, R. H., & Conroy, C. 2013, *ApJ*, **770**, 57
- Bertin, E., & Arnouts, S. 1996, *A&AS*, **117**, 393
- Bertin, E., Mellier, Y., Radovich, M., et al. 2002, in ASP Conf. Ser. 281, *Astronomical Data Analysis Software and Systems XI*, ed. D. A. Bohlender, D. Durand, & T. H. Handley (San Francisco, CA: ASP), 228
- Bhatawdekar, R., Conselice, C. J., Margalef-Bentabol, B., & Duncan, K. 2019, *MNRAS*, **486**, 3805
- Bland-Hawthorn, J., Sutherland, R., & Webster, D. 2015, *ApJ*, **807**, 154
- Bouché, N., Dekel, A., Genzel, R., et al. 2010, *ApJ*, **718**, 1001
- Bouchet, P., García-Marín, M., Lagage, P. O., et al. 2015, *PASP*, **127**, 612
- Bouwens, R., González-López, J., Aravena, M., et al. 2020, *ApJ*, **902**, 112
- Bouwens, R. J., Illingworth, G. D., Ellis, R. S., Oesch, P. A., & Stefanon, M. 2022a, *ApJ*, **940**, 55
- Bouwens, R. J., Illingworth, G. D., Oesch, P. A., et al. 2014, *ApJ*, **793**, 115
- Bouwens, R. J., Illingworth, G. D., Oesch, P. A., et al. 2015, *ApJ*, **803**, 34
- Bouwens, R. J., Oesch, P. A., Illingworth, G. D., Ellis, R. S., & Stefanon, M. 2017, *ApJ*, **843**, 129
- Bouwens, R. J., Oesch, P. A., Stefanon, M., et al. 2021, *AJ*, **162**, 47
- Bouwens, R. J., Stefanon, M., Brammer, G., et al. 2022b, arXiv:2211.02607
- Bowler, R. A. A., Dunlop, J. S., McLure, R. J., et al. 2014, *MNRAS*, **440**, 2810
- Bowler, R. A. A., Jarvis, M. J., Dunlop, J. S., et al. 2020, *MNRAS*, **493**, 2059
- Boyer, M. L., Anderson, J., Gennaro, M., et al. 2022, *RNAAS*, **6**, 191
- Boyle, K., Mascia, S., Pentericci, L., et al. 2022, *ApJL*, **940**, L52
- Broadhurst, T., Benítez, N., Coe, D., et al. 2005, *ApJ*, **621**, 53
- Bunker, A. J. 2020, in IAU Symp. 352, *Uncovering Early Galaxy Evolution in the ALMA and JWST Era*, ed. E. da Cunha et al. (Cambridge: Cambridge Univ. Press), 342
- Calzetti, D., Armus, L., Bohlin, R. C., et al. 2000, *ApJ*, **533**, 682
- Caminha, G. B., Suyu, S. H., Mercurio, A., et al. 2022, *A&A*, **666**, L9
- Carnall, A. C., Bagley, M., McLeod, D. J., et al. 2023, *MNRAS*, **518**, L45
- Castellano, M., Fontana, A., Treu, T., et al. 2022, *ApJL*, **938**, L15
- Chabrier, G. 2003, *PASP*, **115**, 763
- Cheng, C., Yan, H., Huang, J.-S., et al. 2022, *ApJL*, **936**, L19
- Choi, J., Conroy, C., & Byler, N. 2017, *ApJ*, **838**, 159
- Choi, J., Dotter, A., Conroy, C., et al. 2016, *ApJ*, **823**, 102
- Chon, S., Ono, H., Omukai, K., & Schneider, R. 2022, *MNRAS*, **514**, 4639
- Coe, D., Salmon, B., Bradač, M., et al. 2019, *ApJ*, **884**, 85
- Coleman, G. D., Wu, C. C., & Weedman, D. W. 1980, *ApJS*, **43**, 393
- Conroy, C., & Gunn, J. E. 2010, *ApJ*, **712**, 833
- Conroy, C., Gunn, J. E., & White, M. 2009, *ApJ*, **699**, 486
- Cowie, L. L., Lilly, S. J., Gardner, J., & McLean, I. S. 1988, *ApJL*, **332**, L29
- Curti, M., D'Eugenio, F., Carniani, S., et al. 2023, *MNRAS*, **518**, 425
- Dayal, P., & Ferrara, A. 2018, *PhR*, **780**, 1
- Dayal, P., Ferrara, A., Dunlop, J. S., & Paccucci, F. 2014, *MNRAS*, **445**, 2545
- Dayal, P., Rossi, E. M., Shiralilou, B., et al. 2019, *MNRAS*, **486**, 2336
- de Barros, S., Schaerer, D., & Stark, D. P. 2014, *A&A*, **563**, A81
- Donnan, C. T., McLeod, D. J., Dunlop, J. S., et al. 2023, *MNRAS*, **518**, 6011
- Doyon, R., Hutchings, J. B., Beaulieu, M., et al. 2012, *Proc. SPIE*, **8442**, 84422R
- Dunlop, J. S., Abraham, R. G., Ashby, M. L. N., et al. 2021, JWST Proposal 1837
- Ferreira, L., Adams, N., Conselice, C. J., et al. 2022, *ApJL*, **938**, L2
- Finkelstein, S. L., Bagley, M., Song, M., et al. 2022a, *ApJ*, **928**, 52
- Finkelstein, S. L., Bagley, M. B., Arrabal Haro, P., et al. 2022b, *ApJL*, **940**, L55
- Finkelstein, S. L., Bagley, M. B., Ferguson, H. C., et al. 2022c, arXiv:2211.05792
- Finkelstein, S. L., Dickinson, M., Ferguson, H. C., et al. 2017, JWST Proposal, 1345
- Finkelstein, S. L., Ryan, R. E., Jr., Papovich, C., et al. 2015a, *ApJ*, **810**, 71
- Finkelstein, S. L., Song, M., Behroozi, P., et al. 2015b, *ApJ*, **814**, 95
- Foreman-Mackey, D., Hogg, D. W., Lang, D., & Goodman, J. 2013, *PASP*, **125**, 306
- Fox, C., Mahler, G., Sharon, K., & Remolina González, J. D. 2022, *ApJ*, **928**, 87
- Fujimoto, S., Finkelstein, S. L., Burgarella, D., et al. 2022, arXiv:2211.03896
- Gehrels, N. 1986, *ApJ*, **303**, 336
- Giavalisco, M. 2002, *ARA&A*, **40**, 579
- Giavalisco, M., Ferguson, H. C., Koekemoer, A. M., et al. 2004, *ApJL*, **600**, L93
- Golubchik, M., Furtak, L. J., Meena, A. K., & Zitrin, A. 2022, *ApJ*, **938**, 14
- Grogin, N. A., Kocevski, D. D., Faber, S. M., et al. 2011, *ApJS*, **197**, 35
- Harikane, Y., Inoue, A. K., Mawatari, K., et al. 2022a, *ApJ*, **929**, 1
- Harikane, Y., Ono, Y., Ouchi, M., et al. 2022b, *ApJS*, **259**, 20
- Harikane, Y., Ouchi, M., Ono, Y., et al. 2016, *ApJ*, **821**, 123
- Harikane, Y., Ouchi, M., Ono, Y., et al. 2018, *PASJ*, **70**, S11
- Hashimoto, T., Laporte, N., Mawatari, K., et al. 2018, *Natur*, **557**, 392
- Hilbert, B., Sahlmann, J., Volk, K., et al. 2019, spacetelescope/mirage: First Github Release, v2.1.0, Zenodo, doi:10.5281/zenodo.3519262
- Hirano, S., Hosokawa, T., Yoshida, N., et al. 2014, *ApJ*, **781**, 60
- Hirano, S., Hosokawa, T., Yoshida, N., Omukai, K., & Yorke, H. W. 2015, *MNRAS*, **448**, 568
- Hoefl, M., Yepes, G., Gottlöber, S., & Springel, V. 2006, *MNRAS*, **371**, 401
- Inayoshi, K., Harikane, Y., Inoue, A. K., Li, W., & Ho, L. C. 2022, *ApJL*, **938**, L10
- Inoue, A. K., Shimizu, I., Iwata, I., & Tanaka, M. 2014, *MNRAS*, **442**, 1805
- Ishigaki, M., Kawamata, R., Ouchi, M., et al. 2015, *ApJ*, **799**, 12
- Ishigaki, M., Kawamata, R., Ouchi, M., et al. 2018, *ApJ*, **854**, 73
- Jakobsen, P., Ferruit, P., Alves de Oliveira, C., et al. 2022, *A&A*, **661**, A80
- Jiang, L., Kashikawa, N., Wang, S., et al. 2021, *NatAs*, **5**, 256
- Johnson, B. D., Leja, J., Conroy, C., & Speagle, J. S. 2021, *ApJS*, **254**, 22
- Jullo, E., Kneib, J. P., Limousin, M., et al. 2007, *NJPh*, **9**, 447
- Kartaltepe, J., Casey, C. M., Bagley, M., et al. 2021, JWST Proposal, 1727
- Kawamata, R., Ishigaki, M., Shimasaku, K., et al. 2018, *ApJ*, **855**, 4
- Kawamata, R., Oguri, M., Ishigaki, M., Shimasaku, K., & Ouchi, M. 2016, *ApJ*, **819**, 114
- Kirkpatrick, J. D., Cushing, M. C., Gelino, C. R., et al. 2011, *ApJS*, **197**, 19
- Koekemoer, A. M., Faber, S. M., Ferguson, H. C., et al. 2011, *ApJS*, **197**, 36
- Kroupa, P. 2001, *MNRAS*, **322**, 231
- Labbe, I., Bezanson, R., Atek, H., et al. 2021, JWST Proposal, 2561
- Laporte, N., Infante, L., Troncoso Iribarren, P., et al. 2016, *ApJ*, **820**, 98
- Leethochawalit, N., Roberts-Borsani, G., Morishita, T., Trenti, M., & Treu, T. 2022, arXiv:2205.15388
- Livermore, R. C., Finkelstein, S. L., & Lotz, J. M. 2017, *ApJ*, **835**, 113
- Lotz, J. M., Koekemoer, A., Coe, D., et al. 2017, *ApJ*, **837**, 97
- Lovell, C. C., Vijayan, A. P., Thomas, P. A., et al. 2021, *MNRAS*, **500**, 2127
- Madau, P. 1995, *ApJ*, **441**, 18
- Madau, P., & Dickinson, M. 2014, *ARA&A*, **52**, 415
- Mahler, G., Jauzac, M., Richard, J., et al. 2022, arXiv:2207.07101
- Marchesini, D., Brammer, G., Morishita, T., et al. 2023, *ApJL*, **942**, L25
- Mason, C. A., Trenti, M., & Treu, T. 2015, *ApJ*, **813**, 21
- Mason, C. A., Trenti, M., & Treu, T. 2023, *MNRAS*, in press
- Mawatari, K., Inoue, A. K., Hashimoto, T., et al. 2020a, *ApJ*, **889**, 137
- Mawatari, K., Inoue, A. K., Yamanaka, S., Hashimoto, T., & Tamura, Y. 2020b, in IAU Symp. 341, *Challenges in Panchromatic Modelling with Next Generation Facilities*, ed. M. Boquien et al. (Cambridge: Cambridge Univ. Press), 285
- McLeod, D. J., McLure, R. J., & Dunlop, J. S. 2016, *MNRAS*, **459**, 3812
- Mesinger, A., Bryan, G. L., & Haiman, Z. 2009, *MNRAS*, **399**, 1650
- Meurer, G. R., Heckman, T. M., & Calzetti, D. 1999, *ApJ*, **521**, 64
- Morishita, T., & Stiavelli, M. 2022, arXiv:2207.11671
- Morishita, T., Trenti, M., Stiavelli, M., et al. 2018, *ApJ*, **867**, 150
- Mortlock, D. J., Warren, S. J., Venemans, B. P., et al. 2011, *Natur*, **474**, 616
- Moster, B. P., Naab, T., & White, S. D. M. 2013, *MNRAS*, **428**, 3121
- Moster, B. P., Naab, T., & White, S. D. M. 2018, *MNRAS*, **477**, 1822
- Naidu, R. P., Oesch, P. A., Setton, D. J., et al. 2022a, arXiv:2208.02794
- Naidu, R. P., Oesch, P. A., van Dokkum, P., et al. 2022b, *ApJL*, **940**, L14

- Nakajima, K., & Maiolino, R. 2022, *MNRAS*, **513**, 5134
- Nakajima, K., Ouchi, M., Isobe, Y., et al. 2023, arXiv:2301.12825
- Navarro, J. F., Frenk, C. S., & White, S. D. M. 1997, *ApJ*, **490**, 493
- Oesch, P. A., Bouwens, R. J., Illingworth, G. D., et al. 2013, *ApJ*, **773**, 75
- Oesch, P. A., Bouwens, R. J., Illingworth, G. D., Labbé, I., & Stefanon, M. 2018, *ApJ*, **855**, 105
- Oesch, P. A., Brammer, G., van Dokkum, P. G., et al. 2016, *ApJ*, **819**, 129
- Oguri, M. 2010, *PASJ*, **62**, 1017
- Oguri, M. 2021, *PASP*, **133**, 074504
- Oke, J. B., & Gunn, J. E. 1983, *ApJ*, **266**, 713
- Omukai, K., Tsuribe, T., Schneider, R., & Ferrara, A. 2005, *ApJ*, **626**, 627
- Ono, Y., Harikane, Y., Ouchi, M., et al. 2022, arXiv:2208.13582
- Ono, Y., Ouchi, M., Curtis-Lake, E., et al. 2013, *ApJ*, **777**, 155
- Ono, Y., Ouchi, M., Harikane, Y., et al. 2018, *PASJ*, **70**, S10
- Ouchi, M., Mobasher, B., Shimasaku, K., et al. 2009, *ApJ*, **706**, 1136
- Ouchi, M., Ono, Y., & Shibuya, T. 2020, *ARA&A*, **58**, 617
- Pacucci, F., Dayal, P., Harikane, Y., Inoue, A. K., & Loeb, A. 2022, *MNRAS*, **514**, L6
- Pagul, A., Sánchez, F. J., Davidzon, I., & Mobasher, B. 2021, *ApJS*, **256**, 27
- Pascale, M., Frye, B., Diego, J., et al. 2022, *ApJL*, **938**, L6
- Patten, B. M., Stauffer, J. R., Burrows, A., et al. 2006, *ApJ*, **651**, 502
- Pawlik, A. H., & Schaye, J. 2009, *MNRAS*, **396**, L46
- Peng, C. Y., Ho, L. C., Impey, C. D., & Rix, H.-W. 2010, *AJ*, **139**, 2097
- Planck Collaboration, Aghanim, N., Akrami, Y., et al. 2020, *A&A*, **641**, A6
- Rieke, M. J., Kelly, D., & Horner, S. 2005, *Proc. SPIE*, **5904**, 1
- Roberts-Borsani, G., Morishita, T., Treu, T., et al. 2022, *ApJL*, **938**, L13
- Robertson, B. E. 2022, *ARA&A*, **60**, 121
- Rojas-Ruiz, S., Finkelstein, S. L., Bagley, M. B., et al. 2020, *ApJ*, **891**, 146
- Salpeter, E. E. 1955, *ApJ*, **121**, 161
- Sawala, T., Scannapieco, C., Maio, U., & White, S. 2010, *MNRAS*, **402**, 1599
- Schaerer, D., & de Barros, S. 2009, *A&A*, **502**, 423
- Schaerer, D., & de Barros, S. 2010, *A&A*, **515**, A73
- Schaerer, D., Marques-Chaves, R., Oesch, P., et al. 2022, *A&A*, **665**, L4
- Schlafly, E. F., & Finkbeiner, D. P. 2011, *ApJ*, **737**, 103
- Schlegel, D. J., Finkbeiner, D. P., & Davis, M. 1998, *ApJ*, **500**, 525
- Scoville, N., Abraham, R. G., Aussel, H., et al. 2007, *ApJS*, **172**, 38
- Shibuya, T., Miura, N., Iwadate, K., et al. 2022, *PASJ*, **74**, 73
- Shibuya, T., Ouchi, M., & Harikane, Y. 2015, *ApJS*, **219**, 15
- Somerville, R. S., Lee, K., Ferguson, H. C., et al. 2004, *ApJL*, **600**, L171
- Somerville, R. S., Olsen, C., Yung, L. Y. A., et al. 2021, *MNRAS*, **502**, 4858
- Stark, D. P. 2016, *ARA&A*, **54**, 761
- Stefanon, M., Labbé, I., Bouwens, R. J., et al. 2019, *ApJ*, **883**, 99
- Steidel, C. C., Adelberger, K. L., Giavalisco, M., Dickinson, M., & Pettini, M. 1999, *ApJ*, **519**, 1
- Steidel, C. C., Giavalisco, M., Pettini, M., Dickinson, M., & Adelberger, K. L. 1996, *ApJL*, **462**, L17
- Stevans, M. L., Finkelstein, S. L., Wold, I., et al. 2018, *ApJ*, **863**, 63
- Suess, K. A., Bezanson, R., Nelson, E. J., et al. 2022, *ApJL*, **937**, L33
- Susa, H., & Umemura, M. 2004, *ApJ*, **600**, 1
- Tacchella, S., Bose, S., Conroy, C., Eisenstein, D. J., & Johnson, B. D. 2018, *ApJ*, **868**, 92
- Tacchella, S., Finkelstein, S. L., Bagley, M., et al. 2022, *ApJ*, **927**, 170
- Teplitz, H. I., Rafelski, M., Kurczynski, P., et al. 2013, *AJ*, **146**, 159
- Treu, T., Roberts-Borsani, G., Bradac, M., et al. 2022, *ApJ*, **935**, 110
- Treu, T. L., Abramson, L. E., Bradac, M., et al. 2017, JWST Proposal 1324
- Vijayan, A. P., Lovell, C. C., Wilkins, S. M., et al. 2021, *MNRAS*, **501**, 3289
- Wang, F., Yang, J., Fan, X., et al. 2021, *ApJL*, **907**, L1
- Wang, X., Jones, T., Vulcani, B., et al. 2022, *ApJL*, **938**, L16
- Wilkins, S. M., Vijayan, A. P., Lovell, C. C., et al. 2023, *MNRAS*, **519**, 3118
- Williams, R. E., Blacker, B., Dickinson, M., et al. 1996, *AJ*, **112**, 1335
- Windhorst, R. A., Cohen, S. H., Hathi, N. P., et al. 2011, *ApJS*, **193**, 27
- Yan, H., Ma, Z., Ling, C., et al. 2023, *ApJL*, **942**, L9
- Yang, L., Leethochawalit, N., Treu, T., et al. 2022, *MNRAS*, **514**, 1148
- Yue, B., Ferrara, A., & Xu, Y. 2016, *MNRAS*, **463**, 1968
- Yung, L. Y. A., Somerville, R. S., Ferguson, H. C., et al. 2022, *MNRAS*, **515**, 5416
- Yung, L. Y. A., Somerville, R. S., Finkelstein, S. L., et al. 2020, *MNRAS*, **496**, 4574
- Yung, L. Y. A., Somerville, R. S., Finkelstein, S. L., Popping, G., & Davé, R. 2019, *MNRAS*, **483**, 2983
- Zackrisson, E., Bergvall, N., & Leitet, E. 2008, *ApJL*, **676**, L9
- Zackrisson, E., Rydberg, C.-E., Schaerer, D., Östlin, G., & Tuli, M. 2011, *ApJ*, **740**, 13
- Zavala, J. A., Buat, V., Casey, C. M., et al. 2023, *ApJL*, **943**, L9
- Zitrin, A., Broadhurst, T., Umetsu, K., et al. 2009, *MNRAS*, **396**, 1985
- Zitrin, A., Fabris, A., Merten, J., et al. 2015, *ApJ*, **801**, 44